JGR Atmospheres

RESEARCH ARTICLE
10.1029/2022JD036631

This article is a companion to Cheng et al. (2022), https://doi.org/10.1029/2022JD037803

Key Points:

- Turbulence velocity scale is introduced to represent 3-D turbulence strength in the estimation of dry deposition
- Proven measured friction velocity can be replaced by von Karman constant and turbulence velocity scale product to avoid stability functions
- New formulations based on turbulence velocity scale simulated realistic surface latent heat and ozone deposition fluxes at decadal time scales

Supporting Information:

Supporting Information may be found in the online version of this article.

Correspondence to:

K. Alapaty,
alapaty.kiran@epa.gov

Citation:

Alapaty, K., Cheng, B., Bash, J., Munger, J. W., Walker, J. T., & Arunachalam, S. (2022). Dry deposition methods based on turbulence kinetic energy: 1. Evaluation of various resistances and sensitivity studies using a single-point model. *Journal of Geophysical Research: Atmospheres*, *127*, e2022JD036631. https://doi.org/10.1029/2022JD036631

Received 11 FEB 2022
Accepted 6 OCT 2022

Dry Deposition Methods Based on Turbulence Kinetic Energy: 1. Evaluation of Various Resistances and Sensitivity Studies Using a Single-Point Model

Kiran Alapaty[1], Bin Cheng[2], Jesse Bash[1], J. William Munger[3], John T. Walker[1], and Saravanan Arunachalam[4]

[1]Center for Environmental Measurement and Modeling, Office of Research and Development, U.S. Environmental Protection Agency, Research Triangle Park, NC, USA, [2]Oak Ridge Institute for Science and Education Postdoctoral Fellow in the Office of Research and Development, U.S. Environmental Protection Agency, Research Triangle Park, NC, USA, [3]Harvard School of Engineering and Applied Sciences, Cambridge, MA, USA, [4]Institute for the Environment, The University of North Carolina at Chapel Hill, Chapel Hill, NC, USA

Abstract Different functions are used to account for turbulence strength in the atmospheric boundary layer for different stability regimes. These functions are one of the sources for differences among different atmospheric models' predictions and associated biases. Also, turbulence strength is underrepresented in some of the resistance formulations. To address these issues with dry deposition, firstly we take advantage of three-dimensional (3-D) turbulence information in estimating resistances by proposing and validating a 3-D turbulence velocity scale that is relevant for different stability regimes of boundary layer. Secondly, we hypothesize and validate that friction velocity measured by 3-D sonic anemometer can be effectively replaced by the new turbulence velocity scale multiplied by the von Karman constant. Finally, we (a) present a set of resistance formulations for ozone (O_3) based on the 3-D turbulence velocity scale; (b) intercompare estimations of such resistances with those obtained using existing formulations; and, (c) evaluate simulated O_3 fluxes using a single-point dry deposition model against long-term observations of O_3 fluxes at the Harvard Forest (MA) site. Results indicate that the new resistance formulations work very well in simulating surface latent heat and O_3 fluxes when compared to respective existing formulations and measurements at a decadal time scale. Findings from this research may help to improve the capability of dry deposition schemes for better estimation of dry deposition fluxes and create opportunities for the development of a community dry deposition model for use in regional/global air quality models.

Plain Language Summary Chaotic air motions control the amount of pollutant transfer to the surface during dry conditions, which can impact ecosystems, and is a helpful process that can reduce human exposure to air pollutants. Existing pollutant transfer equations use adjustment methods to account for chaotic air motions for different dry conditions. These methods can be sources of errors in estimating pollutant transfer. To avoid using such methods, we propose and evaluate a new velocity parameter derived from using chaotic air energy, which is estimated using other air parameters. Then, we validate the new velocity parameter using sophisticated instrument measurements for chaotic motions. Further, we assume and prove that a constant fraction of that new velocity parameter can be used to avoid adjustment methods and accurately represent strength of chaotic air motions. Finally, we use that new velocity parameter in developing new equations that estimate ozone transfer via various routes to the surface. We used a computer based tool to validate new equations using decadal measurements of ozone fluidities at the Harvard Forest site. Results indicate that our new equations work very well in estimating pollutant transfer. This research has the potential to help manifest a community science package for use in mathematical models.

1. Introduction

Dry deposition is a two-step transport process of air pollutants from the lowest air layer into a thin air layer surrounding objects, and then via this thin layer to objects on the surface. The first and second transport processes are known respectively as aerodynamic transport and boundary layer (also known as quasi-laminar/viscous layer) transport. Surface uptake can cause changes in the physical and/or chemical state of the underlying objects (e.g., vegetation) depending upon the chemical and/or biological uptake capacity. Usually, the slowest process will determine the total rate of pollutant deposition. Thus, dry deposition plays an important role (e.g., Bash

et al., 2013; Emmerichs et al., 2021; Pleim et al., 2019; Wong et al., 2019) in determining the near surface concentrations of various atmospheric pollutants, and it can even adversely affect an ecosystem (e.g., Munger et al., 1998; Walker et al., 2019; WMO, 2021) at local to global scales, in addition to influencing water and carbon cycling. Furthermore, errors in the estimation of dry deposition can contribute to biases in modeled pollutant concentrations. These biases can further create biases in human health exposure estimates. At finer spatial scales, such biases can affect modeled forage times of insects (e.g., honeybees) via changes in identification of floral volatile scents (biogenic volatile compound emissions) due to scent reactions with pollutants such as ozone, and also can lead to reduced pollination by pollinators (Fuentes et al., 2016). Thus, many research efforts have evaluated the accuracy of modeled dry deposition at global scales (e.g., Clifton et al., 2020; Emmerichs et al., 2021) as well as at regional scales (e.g., Hogrefe et al., 2020). Simulated pollutants' (e.g., ozone (O_3)) concentrations are sensitive to the types of dry deposition schemes used in a model and the differences among formulations can result in differing modeling performances (Wu et al., 2018), even for the same underlying surface and meteorology. Further, when many model inputs were kept the same, several dry deposition schemes used in a global model resulted in differences of 2–5 ppbv of surface O_3 concentrations in the northern hemisphere (Wong et al., 2019). Most of these dry deposition formulations are based on limited measurements while refinements are being made even to date as our knowledge on dry deposition is still evolving (e.g., Emmerichs et al., 2021).

Several dry deposition formulations used in regional and global models during the past three decades are variants of the original scheme proposed by Wesely (1989). The differences among such formulations can be attributed to fine improvements in structure and details of processes represented and/or model's suitability among other factors (Wu et al., 2018). Since different approaches are in use, evaluation of various dry deposition schemes for all pollutants is important but can be challenging and resource consuming. Doing so could remain yet an unsettled research issue.

In general, the main factors for differing dry deposition estimates from several global and regional models can primarily be attributed to differences (a) in the number of pathways considered for deposition; (b) among respective formulations; (c) in the specification of surface characteristics including spatial resolution; and, (d) in meteorological inputs. Though each method is scientifically validated, it may be in the best interest of regional and global modeling researchers to have a community version of dry deposition model. It should be computationally viable and covers all possible aspects of dry deposition pathways. Also, it will provide options to choose from an array of resistances suiting the particular needs of a research project. Thus, factors 1 and 2 identified above can be eliminated, thereby reducing the degrees of freedom of the deposition modeling system. The atmospheric modeling community has greatly benefited from the concept of community schemes. For example, the Rapid Radiative Transfer Model for General Circulation Model (GCM) (RRTMG) has become the most widely used radiation scheme in weather and climate modeling studies at regional and global scales (Iacono, 2011). For air pollution modeling, in collaboration with other researchers, the United States Environmental Protection Agency (Pye et al., 2021) is leading the development of a new chemical mechanism, Community Regional Atmospheric Chemistry Multiphase Mechanism (CRACMM), designed for the prediction of multiple endpoints including ozone (O_3), secondary organic aerosol, and toxics linked to cancer and respiratory diseases. The CRACMM will prioritize conservation of emitted mass, transparency in aggregation of species, and offer a platform to integrate contributions from partners. An advantage of such paradigms is that future research efforts can be concentrated on these “community formulations” so that scientific advancements can be accelerated.

Depending upon pollutant types as well as location and time, various deposition pathways can contribute differently to the total deposition. For some of these pathways, atmospheric turbulence is the most important process contributing to the dry deposition and is a function of stability of the planetary boundary layer (PBL). Monin-Obukov Similarity Theory is typically used to represent stability conditions (Toyota et al., 2016). Different schemes use different functions, and many are based on either friction velocity and/or mean wind speed and the Obukhov length (e.g., Flechard et al., 2011; Zhang et al., 2003). Surface wind estimation using friction velocity alone is applicable only for neutral conditions, but for other PBL conditions the current modeling approaches heavily depend on different stability functions to account for differing strengths of turbulence. These approaches partly contribute to differences among different models' predictions and associated biases. A major advantage of using measured friction velocity by 3-D sonic anemometer in 0-D and 1-D models is that it does contain turbulence effects on air flows for all PBL stability regimes, and thus there is no need to use any stability parameter. However, such measurements are continuously available only at couple of sites (e.g., in the US) and cannot provide needed data for regional and global meteorological and air quality models. Therefore, if we produce a

3-D turbulence velocity scale based on the 3-D turbulence information (i.e., variances of velocity fluctuations), then such velocity scale can be a natural parameter to represent 3-D turbulence effects on atmospheric processes.

In air quality models, differences in various stability functions also contribute to the differences in the dry deposition estimates by various formulations. For example, different types of formulations for aerodynamic resistance (R_a) were well evaluated (e.g., Liu et al., 2007), which show that the most crucial parameters in the estimation of R_a were roughness lengths for momentum, heat transfer, and wind speed. In those formulations, different stability functions and constants were used, partly contributing to the differences in the resistance estimations. Similarly, several different formulations for quasi-laminar boundary layer resistance (R_b) and for other resistances exist (e.g., Nemitz et al., 2001; Wesely, 1989), in which turbulence parameters were revised as per the needs of each study. The differences in turbulence parameters in turn can lead to differences in estimations of dry deposition. In a detailed study, Clifton et al. (2020) concluded that O_3 deposition fundamentally depended on turbulence and how it was deduced, and current models do not capture the turbulent transport accurately in the estimation of O_3 fluxes. In a statistical study based on observations, El-Madany et al. (2017) found that the most important driver for the non-stomatal deposition of O_3 was friction velocity. Thus, it can be pointed out that (a) turbulence magnitude plays a vital role in dry deposition and (b) there is a need to develop a methodology that can utilize the three-dimensional (3-D) turbulence information to estimate resistances for use in 3-D air quality models. As a first step, our study focuses on these two important points) by considering surface turbulence kinetic energy (TKE). By using TKE, a velocity scale can be developed to include 3-D turbulence generated during all conditions in the PBL. Thus, the 3-D turbulence-dependent velocity scale can open doors for developing generalized resistance formulations that depend on total turbulence and do not require explicit stability corrections. Therefore, the global objective of our work is to put forward the concept of community dry deposition modeling formulations. This study (Part-1) sets its focus only on a set of resistance formulations for gas deposition that are functions of turbulence while in the companion paper (Part-2) we propose and evaluate resistance formulations for particle deposition. In a near future study, we plan to extend this research to cover all the other resistance formulations not covered in this study. In our future work, we will also evaluate the proposed resistance schemes in a 3-D air quality model using measured O_3 concentrations at regional scales.

Specific objectives of this research are to (a) propose a set of 3-D turbulence-dependent resistance formulations for gases (i.e., O_3) based on the surface TKE; (b) intercompare the resistance estimations with those obtained using existing formulations; and, (c) evaluate the proposed and existing formulations in simulating O_3 fluxes using long-term observations of O_3 fluxes at Harvard Forest site(MA) using a single-point dry deposition model. Section 2 contains methodology used in the research, Section 3 details measurements used and numerical simulations performed, Section 4 contains results, Section 5 documents the outcome from sensitivity studies, and conclusions are provided in Section 6.

2. Methodology

In this section we present descriptions of a velocity scale based on the surface TKE and its estimation using various bulk boundary layer parameters, resistances formulations based on that velocity scale, and a single-point dry deposition model used for numerical simulations that utilizes existing and new resistance formulations for estimating dry deposition.

2.1. Turbulence Velocity Scale

Almost all gas deposition formulations use friction velocity (u_*) for all stability regimes in the PBL. Different stability parameters are used to account for turbulence generated by buoyancy and/or shear production for convective and stable conditions. Here, we propose a new approach where resistance formulations are functions of turbulence generated by buoyancy and/or shear production for all stability regimes of the boundary layer. It is achieved by using surface TKE approximations so that a single formulation will be suitable for different PBL stability conditions. Mean TKE of eddies near the surface can be written as

$$TKE = \overline{e'^2} = \frac{1}{2}\left(\overline{u'^2} + \overline{v'^2} + \overline{w'^2}\right) \quad (1)$$

where e is mean velocity, u, v, and w respectively are eastward, northward, and vertical components of wind, and superscript *prime* denotes fluctuations. Then, terms on the right-hand side of Equation 1 can be rewritten in terms of respective variance of velocity fluctuations as:

$$\overline{e'^2} = \frac{1}{2}\left(\sigma_u^2 + \sigma_v^2 + \sigma_w^2\right)$$

where σ is standard deviation. Now, we define the turbulence velocity scale (e_*) representative of turbulence created by mechanical and buoyant forces at the surface as:

$$e_* = \sqrt{\overline{e'^2}} = \sqrt{\frac{1}{2}\left(\sigma_u^2 + \sigma_v^2 + \sigma_w^2\right)} \tag{2}$$

As documented in the literature (e.g., Hicks, 1985), velocity variance is a result of independent contributions associated with surface momentum flux and the surface vertical heat flux. Following the findings of Hicks (1985), Wyngaard and Cote (1974), and Wyngaard (1975), these surface velocity variances are related to friction and convection velocity scales. Accordingly, velocity variances can be written as:

$$\sigma_{u,v,w}^2 = a^2 u_*^2 + b^2 w_*^2 + c^2 u_*^2 (-z/L)^{2/3}$$

where a, b, and c are constants, u_* is friction velocity, w_* is convection velocity in boundary layer (defined in Text S1 in the Supporting Information S1), z is altitude (usually taken as thickness of a model's lowest layer or altitude at which measurements are made), and L is the Monin-Obukhov length. From the studies of Hicks (1985) based on the Minnesota Turbulence Experiment (Izumi & Caughey, 1976) and Coral Sea (Warner, 1972) observational data over land and tropical ocean (surfaces with a wide range of roughness) respectively, the above relations are found to be fairly applicable for a set of values for a, b, and c. However, different studies, such as Deardorff (1974), Wyngaard and Cote (1974), Wyngaard (1975), and Mailhot and Benoit (1982) have used different values for these three constants. One set of values that were used and successfully tested was by Alapaty and Alapaty (2001), in which the author developed an eddy diffusivity based PBL scheme for use in meteorology and air quality models. In that PBL scheme eddy diffusivity was made a function of e_* to maintain continuity in the estimated eddy diffusivity when PBL stability regimes changed and for a better PBL modeling. Then, He and Alapaty (2018) adapted that e_* formulation to estimate the subcloud layer velocity scale to improve precipitation predictions with their cumulus convection parameterization scheme (Multi-Scale Kain-Fritsch, MSKF scheme) in a regional meteorological modeling study. Following the study of Alapaty and Alapaty (2001) the new turbulence velocity scale, e_* from the above equations can be rewritten for unstable conditions (i.e., when surface sensible heat flux > 0) in PBL as:

$$e_* = \sqrt{3.8u_*^2 + 0.22w_*^2 + 1.9u_*^2(-z/L)^{2/3}} \tag{3a}$$

and for stable conditions in PBL (surface sensible heat flux < 0):

$$e_* = \sqrt{3.8u_*^2} \tag{3b}$$

One advantage of the above equations is that the parameterized e_* transitions smoothly from one stability regime to another since the second and third terms on the right side of Equation 3a drop out for stable conditions. Neutral conditions (i.e., sensible heat flux = 0) are either very infrequently observed or short-lived, especially for situations where measurement data are averaged for 30 min. Consequently, we found only 21 data points for neutral conditions out of all decadal long measurements used in this work. Since it was not clear from the literature as to how to deal with neutral conditions, we have not made any special case for neutral conditions. However, for neutral conditions that exist rarely, e_* needs to be made equal to u_* as a transition point. The sum of the first and second term on the right-hand side of Equation 3a is equal to the sum of the corresponding two terms in Equation 2, while the third term in Equation 2 is equal to the corresponding third term in Equation 3a, as given below:

$$\frac{1}{2}(\sigma_u^2 + \sigma_v^2) = 3.8u_*^2 + 0.22w_*^2 \tag{4a}$$

$$\frac{1}{2}\sigma_w^2 = 1.9u_*^2(-z/L)^{2/3} \tag{4b}$$

Note that Equation 4b is used to estimate vertical velocity variance, and thus it is not a stability correction function. As mentioned above, in a cumulus convection modeling study linking PBL processes with deep convection processes, He and Alapaty (2018) proposed Equation 3 and found that it worked well for estimating the velocity scale for the subcloud layer when z was used to represent lifting condensation level. However, it was not investigated how well this formulation works when applied to estimating resistances for use in air quality modeling. Furthermore, it was also not clear how well the parameterized e_* in Equation 3 using bulk boundary layer parameters compares with that obtained by Equation 2 using micrometeorological measurements for velocity variances. Thus, this study provides an opportunity to intercompare results obtained from using Equations 2 and 3 and provides a basis for validating the estimation of e_* using Equation 3 and its applicability for dry deposition modeling. As noted earlier, direct measurements of velocity variances used in Equation 2 are only available at very limited sites, and the meteorological and air quality models won't be able to use Equation 2 to calculate e_* as model input. Thus, this research also aims to evaluate how well the bulk parameters used in Equation 3, which are available or estimated from routine measurements, will work to estimate e_*.

2.2. Proposed New Resistance Formulations

2.2.1. Aerodynamic Resistance

The aerodynamic resistance, R_a, is controlled by the level of atmospheric turbulence available to transport pollutants from the air to the surface. In our new formulations we first start with the equation for surface wind speed (U) for neutral conditions, written as:

$$U = \frac{u_*}{k} \ln\left[\frac{z - z_d}{z_0}\right] \tag{5}$$

where u_* is friction velocity, k is the von Karman constant (0.41), z_0 is roughness length and is equal to one-tenth of the canopy height, z is the altitude and is equal to the measurement height, and z_d is zero-plane displacement height. Several formulations added different stability functions to the above equation to account for different stability regimes of the PBL (e.g., Pleim & Ran, 2011; Wesely, 1989; Zhang et al., 2003) and a generic form of the above equation suitable for all conditions in the PBL can be written as:

$$U = \frac{u_*}{k}\left[\ln\left(\frac{z - z_d}{z_0}\right) + \varphi_m\right]$$

where φ_m is a stability correction function. When u_* is obtained from measurements (e.g., 3-D sonic anemometer), then it includes contributions of vertical heat flux for the u_* calculation and thus no stability corrections are needed. If we represent such measured u_* as u_{*_c}, then the surface wind speed for all conditions in the PBL can be estimated as:

$$U = \frac{u_{*c}}{k} \ln\left[\frac{z - z_d}{z_0}\right] \tag{6}$$

The aerodynamic resistance for heat or any trace gas, such as O_3, typically used in single-point models for all conditions in the PBL can be written as:

$$R_a = \frac{U}{u_{*c}^2} = \frac{1}{k u_{*c}} \ln\left[\frac{z - z_d}{z_0}\right] \tag{7}$$

Since e_* is a velocity scale for turbulence for all regimes in the PBL, which is based on the 3-D velocity variances (normal stresses) while u_{*_c} is based on covariances (shear stresses), there is a need to scale e_* before it can be used in the above shown aerodynamic resistance and logarithmic wind profile equations. To be able to use the TKE for aerodynamic resistance, we propose that the aerodynamic conductance, G_a, is proportional to (a) the new velocity scale, e_* and (b) intensity of the turbulence, I_t as:

$$G_a \propto e_*$$

$$G_a \propto I_t$$

Here I_t acts like an efficiency term for conductance and e_* acts like an efficacy term. Since e_* is related to the standard deviation of the 3-D velocity fluctuations, it represents the strength of the turbulence and is referred to as the efficacy term. Since larger (smaller) e_* values represent higher (lower) level of turbulence and for a given horizontal wind speed, the intensity of turbulence (ratio of e_* and wind speed) reflects the efficiency of turbulence. It usually varies from 0 to 1 (see Figure S1 in the Supporting Information S1) while values little higher than 1 are possible (due to windspeeds being slightly lower than turbulence velocity that potentially occur during stable conditions) but are not routinely common for surface layer flows. Next, we need a pair of nondimensional constants of proportionality to estimate the aerodynamic conductance. We have considered all known nondimensional parameters that are routinely used in the boundary layer modeling such as the bulk Richardson number, von Karman constant, Prandtl number, and other constants. Based on a simple scale analysis, we hypothesize (and proved in the subsequent Section) that the von Karman constant (k) is the best suited parameter, which is nondimensional and stability independent parameter. Since I_t at the surface usually varies between zero to about 1 and e_* varies from a small value (e.g., 0.1 m s^{-1}) to 2–3 m s^{-1}, usage of k for each of these parameters can yield estimated G_a to be comparable to that obtained from measurements. Thus, we propose to select the von Karman constant as the scaling parameter in the estimation of the new aerodynamic conductance. Then, a new equation for G_a can be written as:

$$G_a = k^2 e_* I_t$$

where I_t is defined as

$$I_t = \frac{e_*}{U}$$

Then, the new aerodynamic resistance equation can be written as

$$R_a = \frac{1}{G_a} = \frac{U}{k^2 e_*^2} = \frac{1}{k^2 e_*} \ln\left[\frac{z - z_d}{z_0}\right] \tag{8}$$

Two points worthy of noting here are: (a) it follows that as per our hypothesis $u_{*_c} = k e_*$ and (b) Equation 8 is very similar to the Equation 7, and both can be used for all conditions in the PBL analysis as well as numerical modeling without the need for using any stability functions. Thus, the surface wind speed for all conditions in the PBL can also be estimated as:

$$U = e_* \ln\left[\frac{z - z_d}{z_0}\right] \tag{9}$$

Firstly, it is necessary to verify our hypothesis ($u_{*_c} = k\, e_*$), and secondly to assess the validity of Equation 9 in estimating the surface wind speed. In doing so we also evaluate Equation 6 to study the abilities of these two formulations in replicating observed wind speed, which will be presented in the next section.

2.2.2. Boundary Layer Resistance

Resistance to transport through the very thin viscous sub-layer at the surface for leaf and soil are also considered in this study. This thin layer is also referred to as the quasi-laminar layer, laminar deposition layer or boundary layer where transport is fundamentally characterized by molecular diffusion for gases. For this reason, u_* is used traditionally in leaf and soil boundary layer resistance formulations without any stability correction parameters (e.g., Padro et al., 1991). However, this is valid only for neutral conditions. For other conditions, such as daytime with surface heating, the literature indicates the presence of convective plumes at the leaf scale for calm and windy air conditions since plants are subjected to heat load or thermal stress. Convection phenomena from plants in calm and windy air was observationally studied firstly by Gates and Benedict (1962). Using Schlieren photography and other instruments along with an infrared radiation gun, they quantitatively estimated the amount of energy convected away from a leaf under free and forced convection for broad-leaved and coniferous tree needles. Schlieren photography movies showed distinct convective plumes moving away from leaf surface indicating turbulence. In another experimental study, Wigley and Clark (1974) determined the heat transfer from model leaves heated by a constant energy flux under forced convection. In another experimental and field study, Brenner and Jarvis (1995) found that for forced convection conditions, at wind speeds above 2.5 m s^{-1} leaf boundary layer conductances were higher than those for a laminar leaf boundary layer. To account for increased

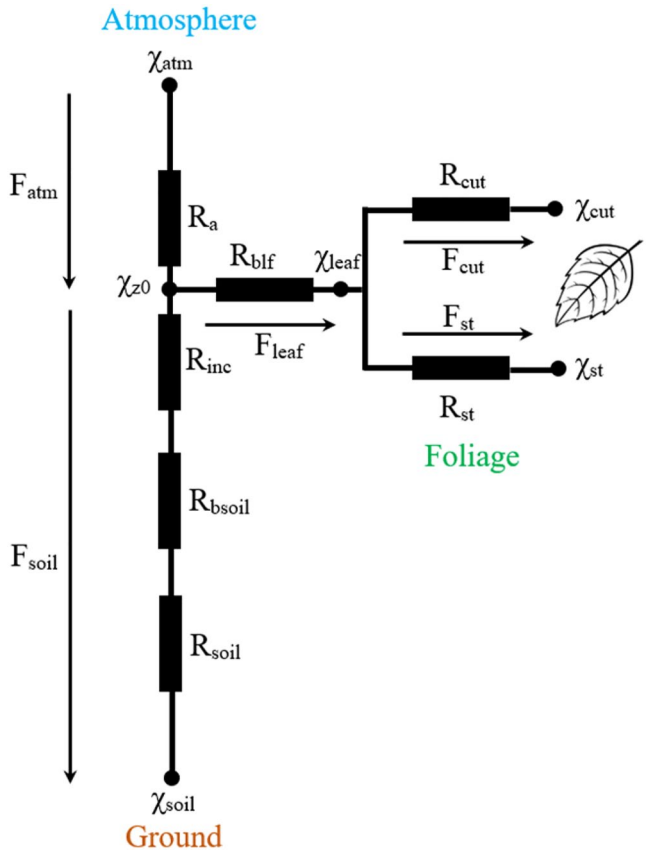

Figure 1. Two-layer foliage/ground resistance model modified from Nemitz et al. (2001) and Stella et al. (2011) adapted for Ozone.

particle deposition under convective conditions in the PBL, Wesely, 1989 have suggested an empirical equation to increase the deposition velocity of sulfate particles by introducing a convection factor in boundary layer resistance formulation. Similarly, soil boundary layer studies also exist (e.g., Kiefer et al., 2008) in the literature. Considering results from these studies, we justify using the product ke_* in the place of u_* even for the leaf and soil boundary layer resistance formulations. Then, the new equations for leaf (R_{blf}) and soil (R_{bsoil}) quasi-laminar boundary layer resistances can be written similar to that reported by Personne et al. (2009) and Massad et al. (2010) as:

$$R_{blf} = \frac{v\left(l_{leaf}\, ke_*/\left(v\, LAI^2\right)\right)^{1/3}}{Dke_*} \tag{10}$$

$$R_{bsoil} = \frac{\frac{v}{D} - log\left\{\frac{10\,D}{k\exp(-LAI*0.5)\,ke_*}\right\}}{k\exp(-LAI*0.5)\,ke_*} = \frac{\frac{v}{D} - log\left\{\frac{10\,D}{k^2\exp(-LAI*0.5)\,e_*}\right\}}{k^2\exp(-LAI*0.5)\,e_*} \tag{11}$$

where u_* in the original formulations is replaced by the product of k *and* e_* as shown in the above new equations, ν is kinematic viscosity of air, l_{leaf} is characteristic leaf width specified as 0.0314 m, LAI is leaf area index, and D is diffusivity of gases. Note that the u_{*_c} obtained from the measurements naturally included contribution of heat loading on leaf/soil surfaces and its impacts on the vertical flux of momentum, thus usage of e_* in the above formulation is consistent with the standard formulations used in our single-point model. It is worthy to note that the 3-D air quality models do not use any stability functions in these resistances and in-canopy resistance; and thus, our new resistance formulations can offer a better approach for these processes.

2.2.3. In-Canopy Aerodynamic Resistance

Since in-canopy aerodynamic resistance (R_{inc}) is a function of aerodynamic resistance in the original formulation, it is impacted by the usage of Equation 3 and is written as:

$$R_{inc} = R_a\left(e^{0.5\,LAI} - 1\right) = \frac{U}{k^2 e_*^2}\left(e^{0.5\,LAI} - 1\right) \tag{12}$$

Thus, in this study, resistances shown in Equations 8 and 10–12 contain the new velocity scale to represent varying strengths of turbulence affecting the magnitude of gas deposition to the surface through the respective pathways. Development of new formulations for particle deposition is reported in the companion paper (Part-2) while the additional surface resistances (e.g., stomatal resistance) will be reported in follow-up research.

2.3. Single-Point Dry Deposition Model

To model the dry deposition of O_3, we use the Surface Tiled Aerosol and Gas Exchange (STAGE) deposition model that is part of the publicly available version of the Community Multiscale Air Quality (CMAQ) Model v5.3 release (Appel et al., 2021). STAGE is constructed as a single-point two-layer exchange model as shown in Figure 1 and it can also be used as bidirectional exchange model.

where F_{atm} is the air-surface exchange of O_3 and F_{soil}, F_{leaf}, F_{st}, and F_{cut} are the in-canopy exchange of O_3 between the soil, leaf, stomata, and cuticle respectively where $F_{atm} = Fsoil + F_{leaf}$ and $F_{leaf} = F_{st} + F_{cut}$ following Krichhoff's first current law, χ_{atm} atmospheric compensation point, χ_{z0} canopy compensation point, χ_{soil} soil compensation point, R_{soil} soil resisatance, χ_{leaf} is leaf compensation point, R_{cut} cuticle resistance, χ_{cut} cuticle compensation point, and χ_{st} stomatal compensation point. Note that the soil, cuticle and stomatal O3 compensation points are set to 0 ppb, thus the fluxes are always depositional. Units: all fluxes in ppb m s^{-1}; compensation point in ppb.

The flux equations were modified from Nemitz et al. (2001) and the downward fluxes (deposition) are denoted as negative values and upward fluxes (emission) are denoted as positive values. Deposition velocity (V_d) is calculated based on the Equation 13:

$$V_d = \left(R_a + \frac{1}{\frac{1}{R_{blf} + \frac{1}{\frac{1}{R_{cut}} + \frac{1}{R_{st}}}} + \frac{1}{R_{grnd}}} \right) - 1 \tag{13}$$

where $R_{grnd} = R_{inc} + R_{bsoil} + R_{soil}$; $R_{st} = R_s + R_m$, R_{st} stands for the total resistance to exchange through stomata, which is the sum of stomatal resistance (R_s) and mesophyll resistance (R_m).

With algebraic transformation, Equation 13 can be rewritten as:

$$V_d = \frac{1 - \frac{\chi_{z0}}{\chi_{atm}}}{R_a}$$

as $F_{atm} = -V_d \times \chi_{atm}$

$$F_{atm} = \frac{1}{R_a} \times (\chi_{z0} - \chi_{atm}) = F_{Stomata} + F_{Cuticle} + F_{Soil}$$

$$F_{Stomata} = R_{st}^{-1} \times (\chi_{st} - \chi_{leaf}) = -R_{st}^{-1} \times \chi_{leaf}$$

$$F_{Cuticle} = R_{cut}^{-1} \times (\chi_{cut} - \chi_{leaf}) = -R_{cut}^{-1} \times \chi_{leaf}$$

$$F_{Soil} = (R_{inc} + R_{bsoil} + R_{soil})^{-1} \times (\chi_{soil} - \chi_{z0}) = -R_{grnd}^{-1} \times \chi_{z0}$$

The above fluxes were reduced from the bidirectional form to the unidirectional "deposition only" form similar to Clifton et al. (2020) by setting the surface concentrations $\chi_{st} = \chi_{cut} = \chi_{soil} = 0$. The formulas used for leaf compensation point (χ_{leaf}) and canopy compensation point (χ_{z0}) follow Massad et al. (2010), as shown in Text S2 of the Supporting Information S1.

3. Measurements, Turbulence Velocity Estimation, and Numerical Simulations

3.1. Long-Term Field Measurements at the Harvard Forest Site

Long-term field measurements available at the Harvard Forest site, MA (42.54 N, 72.18 W, 340 m) were utilized in this study (Clifton et al., 2019; Munger et al., 1996; Wu et al., 2011). Surface latent heat fluxes (LHF) and O_3 flux measurements were used to perform model validation. Surface LHF was measured by the eddy covariance using a LiCor 6262 CO_2/H_2O sensor and details can be found in Moore et al. (1996). The O_3 fluxes were measured by the eddy covariance method using an ethene chemiluminescence O_3 analyzer. Details regarding the O_3 fluxes measurements can be found in Munger et al. (1996) and Clifton et al. (2017, 2019).

Vegetation surrounding the measurement tower comprises of different types (oak, maple, and scattered conifers) with a mean canopy height at about 29 m above ground level. Measurements include air temperature, relative humidity, shortwave radiation, friction velocity, wind speed, sensible and latent heat fluxes, O_3 fluxes, soil moisture, soil temperature, leaf area index, and canopy height. Full details of these measurements can be found in Urbanski et al. (2007), Boose and Gould (1999), Barford et al. (2001), and references cited in these articles while data sets are archived at Munger and Wofsy (2021). The various measurements used in this study are listed in the Table S1 of the Supporting Information S1.

Numerical simulations were performed for about a decade using the single-point model starting from 0500 UTC 28 October 1991 to 0400 UTC 13 December 2000. This research concentrates on atmospheric O_3 as a reference pollutant for the air-plant-soil exchange, which can be integrated into a chemical transport model at regional or global scales.

3.2. Turbulence Velocity Estimation

We now describe the calculation of e_* as implemented in the point-model by using Equation 3. Using the measured wind speed, we first estimate friction velocity as:

$$u_* = \frac{kU}{\ln\left(\frac{z-z_d}{z_0}\right)}$$

where k is the von Karman constant specified as 0.41, U is measured mean wind speed, and z for the Harvard Forest site is 29 m, $z_d = 16.9$ m, and $z_0 = 2.4$ m (Moore et al., 1996). Since convection velocity and the Monin-Obukhov length (see Equation 3) are needed but the data (e.g., surface pressure and boundary layer height) used to calculate these two variables were not overlapping with the measurement time period of other variables. Thus, to fill this data gap, we have extracted surface pressure and boundary layer depth data available from a downscaled regional climate simulation by Otte et al. (2012) for the entire study period. The data for these two parameters are available at hourly temporal resolution consistent with the measurement frequency of other measured data at the Harvard Forest site. Now that the required input data for all the variables is prepared, we can parameterize e_* using the Equation 3 for all stability regimes in the PBL. To study the impacts of using these modeled data, we have performed four sensitivity simulations to study the uncertainties present in the climatological values of these two parameters. An uncertainty of about ±5 mb in the surface pressure (two sensitivity simulations) and ±25% in the boundary layer depth (the other two sensitivity simulations) are considered. Results indicate that 5 mb uncertainty didn't have any impact on the estimated e_*, similarly, 25% uncertainty has little impact on e_* estimations (Figure S2 in the Supporting Information S1).

We have performed decadal simulations for two cases: (a) BASE case where the single-point model was run without any changes to formulations for all resistances, and (b) ESTAR case that used the proposed new resistance formulations shown in Equations 8 and 10–12. Note that some of the inputs needed to estimate e_* at times were missing in the Harvard Forest data, so to keep the number of hours of simulation to be the same in the BASE and ESTAR, we have excluded such missing data also in BASE when developing statistical measures. This way, the numbers of data points used in the statistical analyses are the same in both cases.

Before performing the single-point model simulations it is necessary to study the accuracy of the proposed methodology for estimating e_*, which is presented now. The derivation of Equation 3 is rooted in micrometeorological measurements documented in the literature as discussed in the Section 2. However, to date we have not seen any research in the literature evaluating the accuracy of that methodology when compared to direct measurements by a 3-D sonic anemometer on a decadal time scale. Thus, we have obtained measurements for the velocity variances that were measured by sonic anemometer at the Harvard Forest site. Note that 3-D velocity variance data are quality controlled but not rigorously; however, we have used that data "as is". Using 3-D sonic anemometer measurements of velocity variances in Equation 2, we have estimated e_* and referred to it as e_*-*obs* and compared it with that obtained by Equation 3 which uses bulk parameters for the PBL. Figure 2a shows the scatter plot for e_* (estimated using Equation 3) and e_*-*obs* (estimated using Equation 2) and red line is for regression fit and green line for 1:1 match.

As can be seen from Figure 2a, e_* and e_*-*obs* have an excellent correlation with the coefficient of determination, R^2, of about 0.96 and correlation coefficient, $R = 0.98$ and a slope of about 1.12. This result lays a strong foundation for the validation of the e_* estimation by Equation 3 at decadal timescale and its utility representing 3-D turbulence for use in dry deposition modeling. In addition, Figures 2b and 2c show temporal variation for e_* data (parameterized and measured) for a summer and a winter month of 1994 to bring out features clearly while Figure 2d shows their variability across a decade.

In general, the parameterized e_* closely followed the observed trend of e_*-*obs* in both summer and winter of 1994. However, there were still some differences between parameterized e_* and e_*-*obs*. This kind of behavior is expected because the bulk boundary layer parameters are used to estimate e_*, and thus essentially it is a parameterization having minor differences. In addition, locally measured velocity could be a bit more variable than the bulk boundary layer parameters on account of very small-scale eddies associated with features in the canopy that aren't present in the larger boundary layer. Similar trend is found throughout the decadal period though it may not be readily visible in the Figure 2d. We also note that measured (by 3-D sonic anemometer) turbulence velocity (e_*-*obs*) minimum values can approach zero for many hours while parameterized turbulence velocity (e_*)

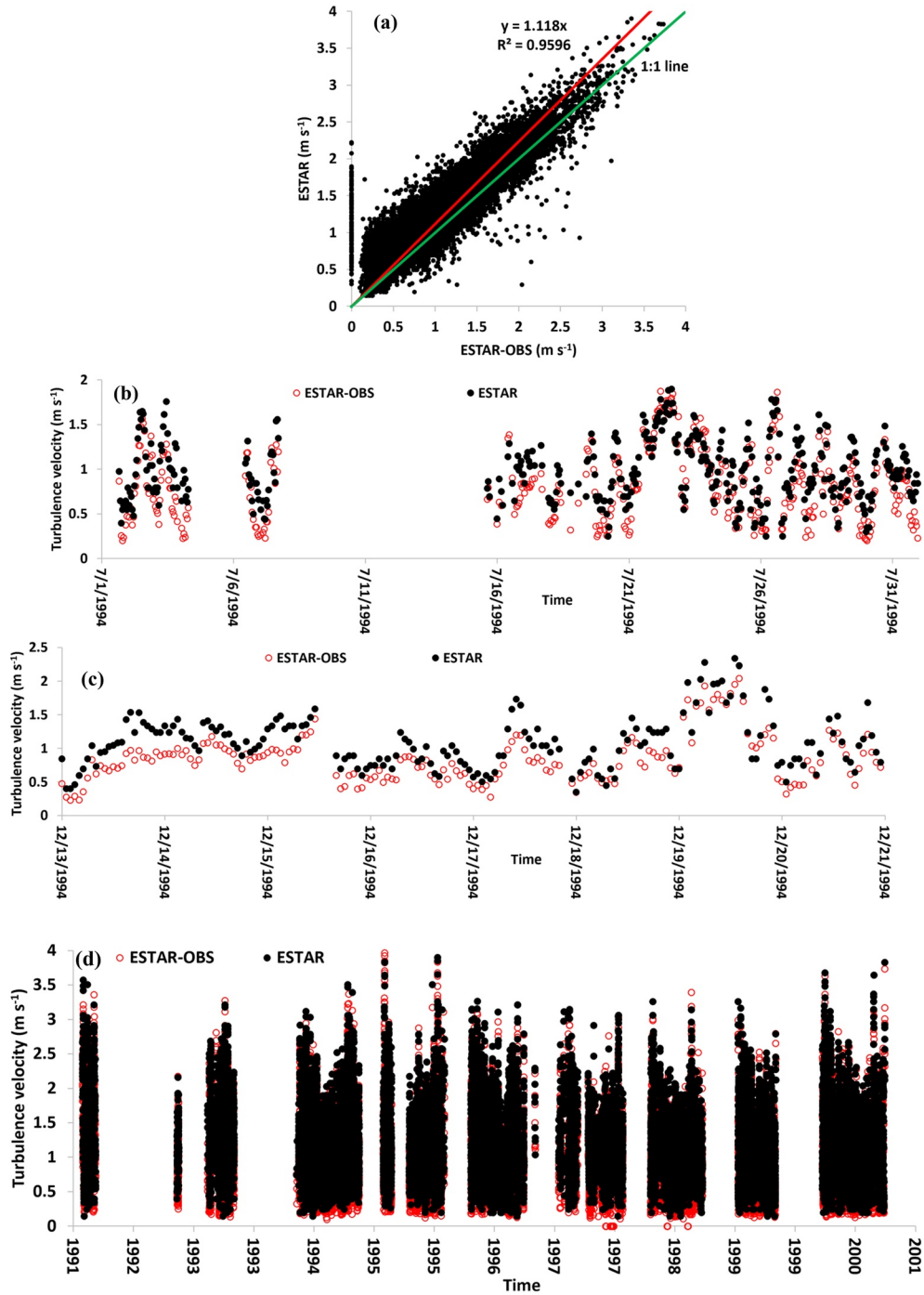

Figure 2. Comparison of observed and parameterized e_* for the decadal period (1991–2000) at the Harvard Forest site: (a) scatter plot of e_* vs e_*-*obs*; (b) temporal variation of e_* and e_*-*obs* for July 1994; (c) temporal variation of e_* and e_*-*obs* for December 1994; and (d) temporal variation of e_* and e_*-*obs* for the decadal period.

minimum values are slightly higher than measured values and are likely representative of stable PBL conditions. To further diagnose the variability of measured and estimated e_*, we stratified the comparisons based on the surface sensible heat flux (H) as a proxy for stability of the PBL. We found that there were 11,707 data points when $H < 0$; and there were 9339 data points when $H > 0$ (Figure S3 in the Supporting Information S1). As found in the Figure 2a, these relationships were very similar for the stable and unstable conditions. These results affirm the validity of the methodology proposed (Equation 3) at a decadal time scale for estimating e_*, which is a

statistically significant result. To the best of our knowledge, this is the first study to utilize measured velocity variances to develop and evaluate a e_* parameterization for use in PBL modeling.

3.3. Estimation of Friction Velocity Using Parameterized Turbulence Velocity Scale

In addition to the comparison between parameterized e_* and measured e_*-*obs* values, we also intercompare the parameterized e_* with the measured friction velocity (u_{*_c}). This comparison will help us to implicitly realize how the magnitudes of normal stresses compare with the shear stresses as shown in Figure 3a as a scatter plot.

Firstly, it will be worthy to detail how observed friction velocity used in BASE was derived from the 3-D sonic anemometer measurements. Friction velocity is computed from the covariance of vertical and horizontal wind velocity measured by the sonic anemometer $u_{*c} = \left\{-\overline{u'w'}\right\}^{0.5}$ after an axis rotation to the data that minimizes the mean crosswind and vertical velocity so the x-axis is aligned with the mean wind (McMillen, 1988). By aligning the u velocity axis with the mean wind, the mean v velocity is 0 and the $\overline{v'w'}$ covariance is negligible (at least three orders of smaller than the covariance $\overline{u'w'}$) and it can be ignored. Since measured friction velocity, i.e., u_{*_c} also includes the effects of turbulence generated by vertical heat flux, there is no need for any stability correction that is typically applied in gridded air pollution models. In a way, the observed u_{*_c} is not truly a friction velocity because it included turbulence generated by the vertical heat flux.

Figure 3a shows a scatter plot of parameterized e_* and observed u_{*_c}. As expected, parameterized e_* is much higher than the u_{*_c}. This is because e_* contains information for 3-D turbulence (i.e., 3-D velocity variances along all axes) while the u_{*_c} contains only a covariance. In other words, the measured friction velocity by a 3-D sonic anemometer contains only vertical transport of horizontal momentum and do not consider vertical transport of vertical momentum. However, variance $\overline{w'^2}$ is accounted for in the estimation of e_* and thus it is larger than measured friction velocity. Since e_* is higher than observed u_{*_c} for almost all data points (except for few), one must expect to introduce a scaling factor for e_* as discussed in the earlier section. The von Karman constant (0.41) provided a good scaling for e_* as can be seen from Figure 3b. There is a strong correlation between observed u_{*_c} and ke_*, with the regression line showing a slope of about 0.95 and R^2 of about 0.94, which is indicative of the potential utilization of e_* for deposition modeling to mimic measured friction velocity that includes effects of vertical heat flux and thereby avoiding explicit usage of a stability function. We also analyzed the slopes and R^2 values for different stability regimes and found that when $H < 0$ (stable) the slope is 0.9764 with a $R^2 = 0.9091$ ($n = 13{,}535$); when $H > 0$ (unstable) the slope is 0.9329 with $R^2 = 0.9648$ ($n = 10{,}622$). Thus, these results directly support our hypothesis that (a) 3-D sonic anemometer measured friction velocity for all conditions in the PBL can be approximated by the product of the von Karman constant and turbulence velocity (ke_*), and (b) the product ke_* can be used to replace u_* in all resistances formulations.

Next, we recalculate surface wind speed using the log-law equations (Equations 6 and 9) since it is another evaluation of e_* if it were to be used in the boundary layer meteorology (which is beyond the scope of this paper). We rewrite Equations 6 and 9 as $U1 = \frac{u_{*c}}{k} \ln\left[\frac{z-z_d}{z_0}\right]$ and $U2 = e_* \ln\left[\frac{z-z_d}{z_0}\right]$ for the sake of referencing. Figures 3c and 3d show the comparison of measured wind speed with U1 and U2. Estimated wind speeds, U1 and U2, compare very well with measured wind speed while U2 aligned a little better with measurements. Since U1 and measured wind speeds are from independent measurements, some scatter is expected but is within the acceptable range of R^2. Estimated U2 values are expected to compare better with the measurements since its origin is related to measured wind speed. The flat distribution of values in U2 following the regression line in Figure 3d (red line) can be associated with stable and weak convective conditions resulting in tighter relationships with measured windspeed.

Since our hypothesis that $u_{*_c} = ke_*$ has been validated, one would expect that U1 should be very similar to U2 and as a verification this relationship is shown in the Figure 3e as a scatter plot. The 1:1 line almost overlaps with the regression line that has a slope of about 0.99. Since U1 and U2 have very similar R^2 and slopes with measurements, it is expected that the U1 vs. U2 to have an excellent slope value since we forced both green and red lines to pass through origin. These results confirm that e_* can be used in the log-law to estimate near surface wind speed in boundary layer modeling and it works for all conditions in the PBL. This result opens doors for a new methodology for surface layer modeling in meteorology that we will address in a near-future research study.

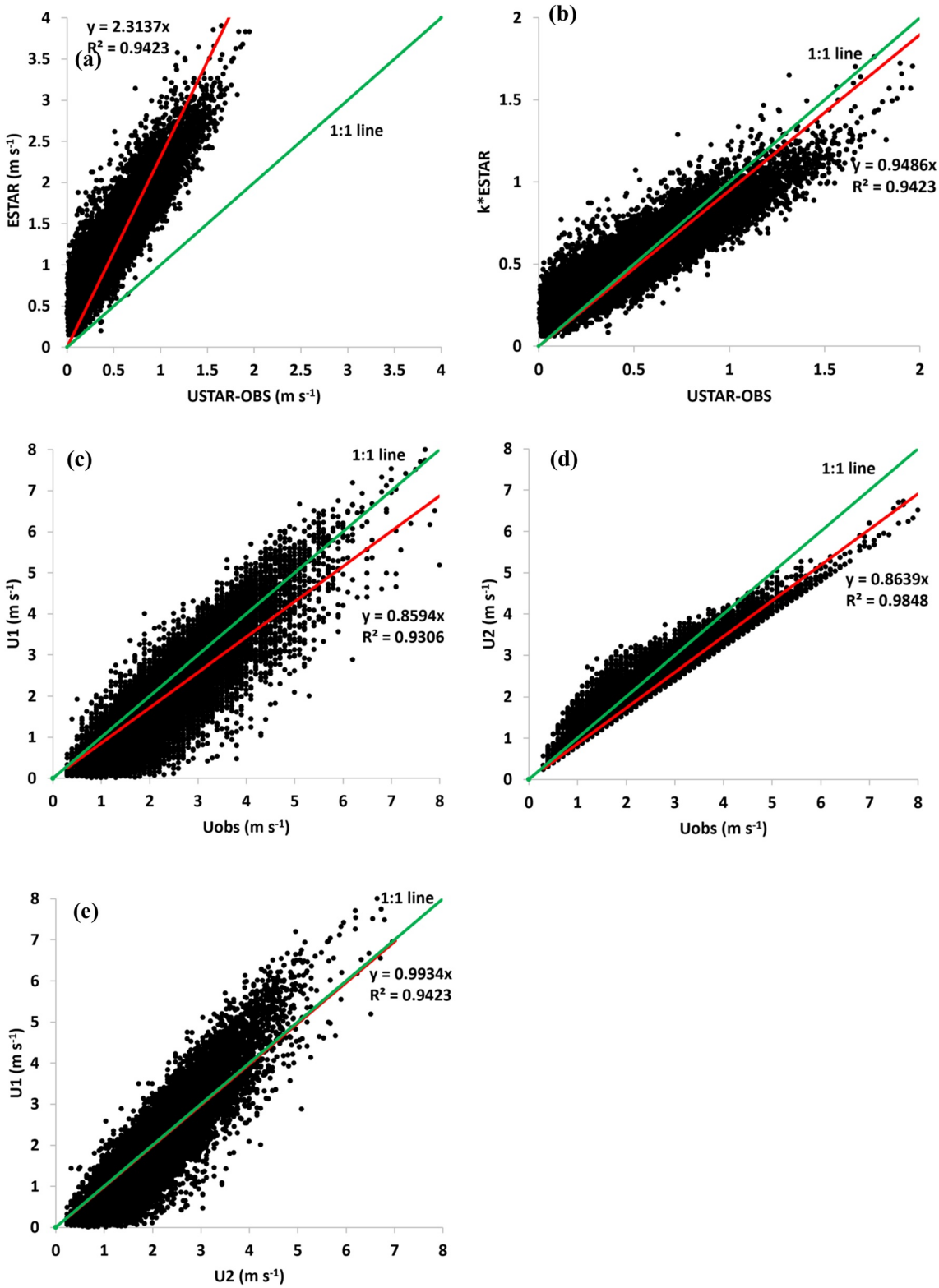

Figure 3. Scatter plot of (a) observed u_{*c} and parameterized e_* (b) observed u_{*c} and ke_* and measured wind speed vs. estimated wind speed using (c) Equation 6, (d) Equation 9, and (e) Equation 6 vs. Equation 9 for the decadal period (1991–2000).

Table 1
Statistical Performance of the Single-Point Model in Estimating Surface Latent Heat Fluxes

Cases	NMB	NME	R	Number of data points
BASE	0.1775	0.6669	0.7065	24,183
ESTAR	0.1940	0.6858	0.7158	24,183

Note. Thus, climatologically, ESTAR has comparable model performance to the BASE, and it is an indication of good model performance in estimating resistances with the new formulations, which is further elaborated in the following sections.

3.4. Surface Latent Heat Fluxes

Surface latent heat fluxes provide a basis to test the ability of our new formulations to estimate various resistances (R_a, R_{blf}, R_{bsoil}, *and* R_{inc}), in this section we present the evaluation of modeled and measured LHF.

Measurements for the surface latent heat fluxes (referred to as OBS) are used to evaluate simulated LHF by BASE and ESTAR. In the single-point model LHF are estimated using Equation 14 where several resistances (R_a, R_{blf}, R_{bsoil}, R_{st}, R_{inc}, and R_{soil}) are used (Figure S4 in the Supporting Information S1). For full details of LHF estimation, see the Text S3 in the Supporting Information S1. Thus, comparison of simulated LHF with those obtained from measurements will provide an evaluation of modeled resistances used in the single-point model. Though this evaluation is not related to evaluation of dry deposition model, which is presented in the following section, but provides an additional opportunity to evaluate new and existing resistance formulations in the single-point model. LHF is estimated as:

$$\mathrm{LHF} = -\frac{q_{vs} - q_{ss\_z0}}{R_a} \times [2.501 - 0.00237(\mathrm{T_a} - 273.15)] \times 10^6 \quad (14)$$

where q_{vs} and q_{ss_zo} are saturation specific humidity in the air and the canopy compensation point of water vapor, respectively; T_a is air temperature (See supplemental information). Richardson et al., 2006 analyzed flux data from Harvard Forest and several other long-term flux measurement network of the Americas (AmeriFlux) sites using a paired observation approach. LHF random error scaled similarly with the magnitude of measured flux at all the forested sites to give a relative error of 23%. Kessomkiat et al. (2013) summarize relative random errors in LHF for several studies/estimation methods and these errors are usually lower during unstable conditions as to stable conditions.

Table 1 shows statistical measures (defined in Text S4 of the Supporting Information S1) for the model performance in predicting the surface LHF. In the ESTAR simulations, predicted LHF are well in line with measurements and the NMB, normalized mean error (NME), and correlation coefficient (R) values are about 0.19, 0.69, and 0.72, respectively. These climatological values of ESTAR are very comparable to those obtained from the BASE simulations. In general, the BASE and ESTAR had very close model performance in predicting LHF when compared to measurements in a decadal period of simulation.

Box plots for decadal averaged diurnal variations of the LHF in Figure 4a showed that estimated LHF in both BASE and ESTAR are similar. In addition, the diurnal variation of the LHF also indicated that both cases overestimated maximum LHF during nighttime while both cases underestimated it from 0700 to about 1200 LT and then both overestimated maximum for the rest of hours. Overestimations in maximum LHF during afternoon hours is quite large with median values far off from measurements. It As per the values shown in Table 1, NMB in both the cases is well below 20% but unfortunately the information on the uncertainty in the measurements does not exist in the literature, making it difficult to quantify the size of errors. Decadal averaged monthly variations of the LHF (Figure 4b) indicated that both BASE and ESTAR overestimated the maximum LHF for cooler months while it is underestimated for warmer months (i.e., June, July, August, and September). Most of the measurements were not accessible for January and February and thus are excluded from model simulations. The above findings are consistent with the statistical analysis of diurnal and monthly model performance for the LHF estimations shown in Figures S3 of the Supporting Information S1. Furthermore, both BASE and ESTAR had very close and very similar model performance (Figure S5 in the Supporting Information S1) during daytime and in warmer months based on the differences and magnitude of NMB, and also for NME and R values shown for both cases. Thus, most of the biases in LHF in both cases can be mainly attributed to simulation errors during nighttime (stable) conditions as canopy could be colder than air and lead to deposition (dew). Moreover, the measured fluxes may be questionable in calm periods because other transport processes may not be negligible relative to turbulent transport. Scatter plot of LHF for BASE *vs.* ESTAR shown in Figure S6 of the Supporting Information S1 exhibited a slope of about 0.97 and R^2 of about 0.98 (and R=0.99). Scatter plots for BASE *vs.* OBS and ESTAR *vs.* OBS (Figure S6 in the Supporting Information S1) also indicated that the ESTAR and BASE performed similarly to each other when compared to OBS. Stomatal resistance is one of the resistances used in

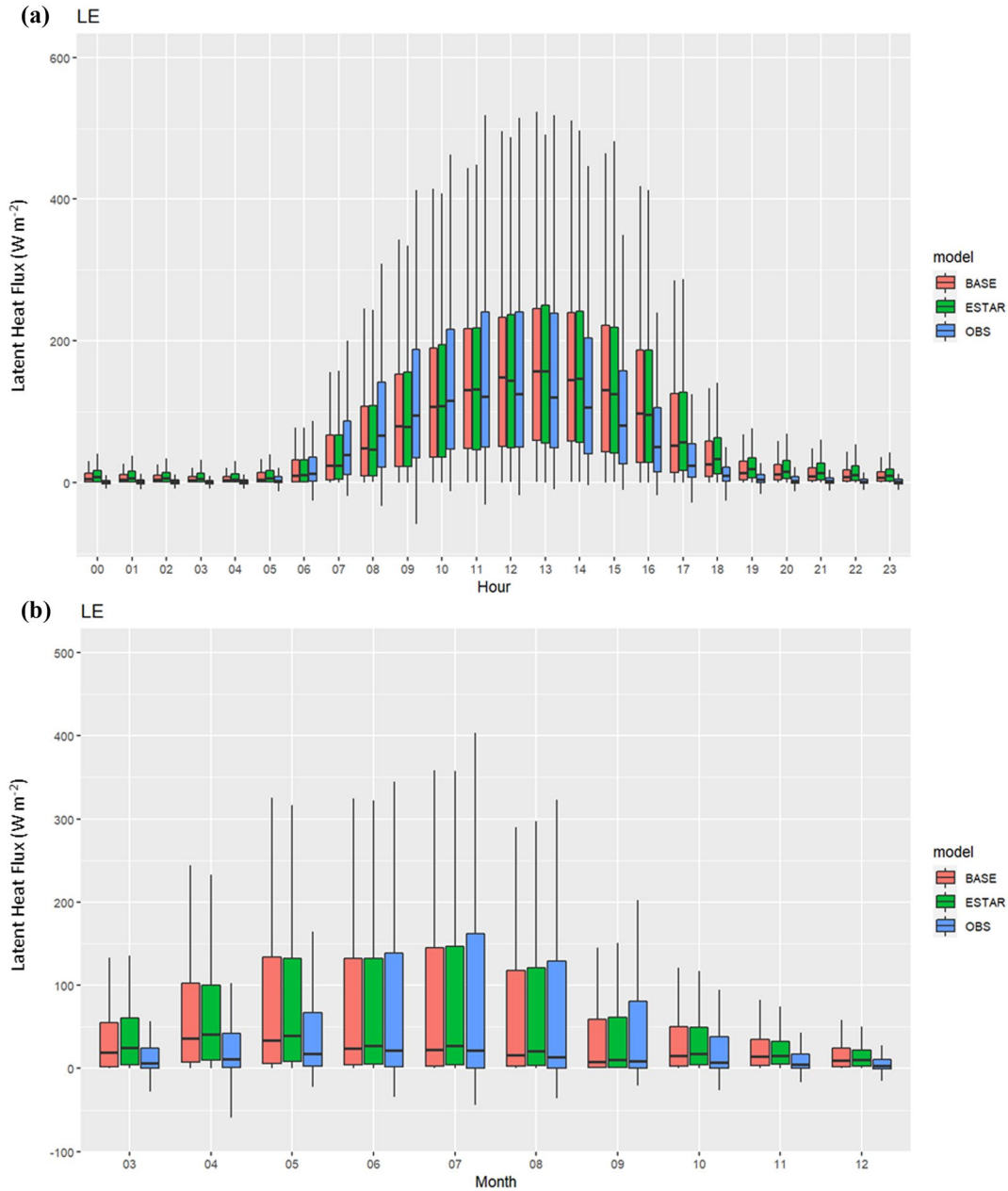

Figure 4. Decadal averaged (a) diurnal and (b) monthly variations of surface latent heat fluxes for BASE, ESTAR, and OBS.

the estimation of LHF and is the dominant parameter during warmer periods in the LHF estimation and it seems to be well characterized given the acceptable size of the LHF biases.

4. Results and Discussions

4.1. Ozone Kinematic Fluxes

Simulated O_3 kinematic fluxes by the BASE and ESTAR were compared with the measurements for the period of 1991–2000. Modeled and observed hourly O_3 fluxes in July and December of 1994 had the best data completeness as compared to other years and are shown in the Figure 5 where negative values indicating deposition. The positive O_3 fluxes occurred during very stable and calm wind conditions that posed challenges to instruments to accurately measure ozone fluxes and is related to instrument limitations of the current technology, thus, positive

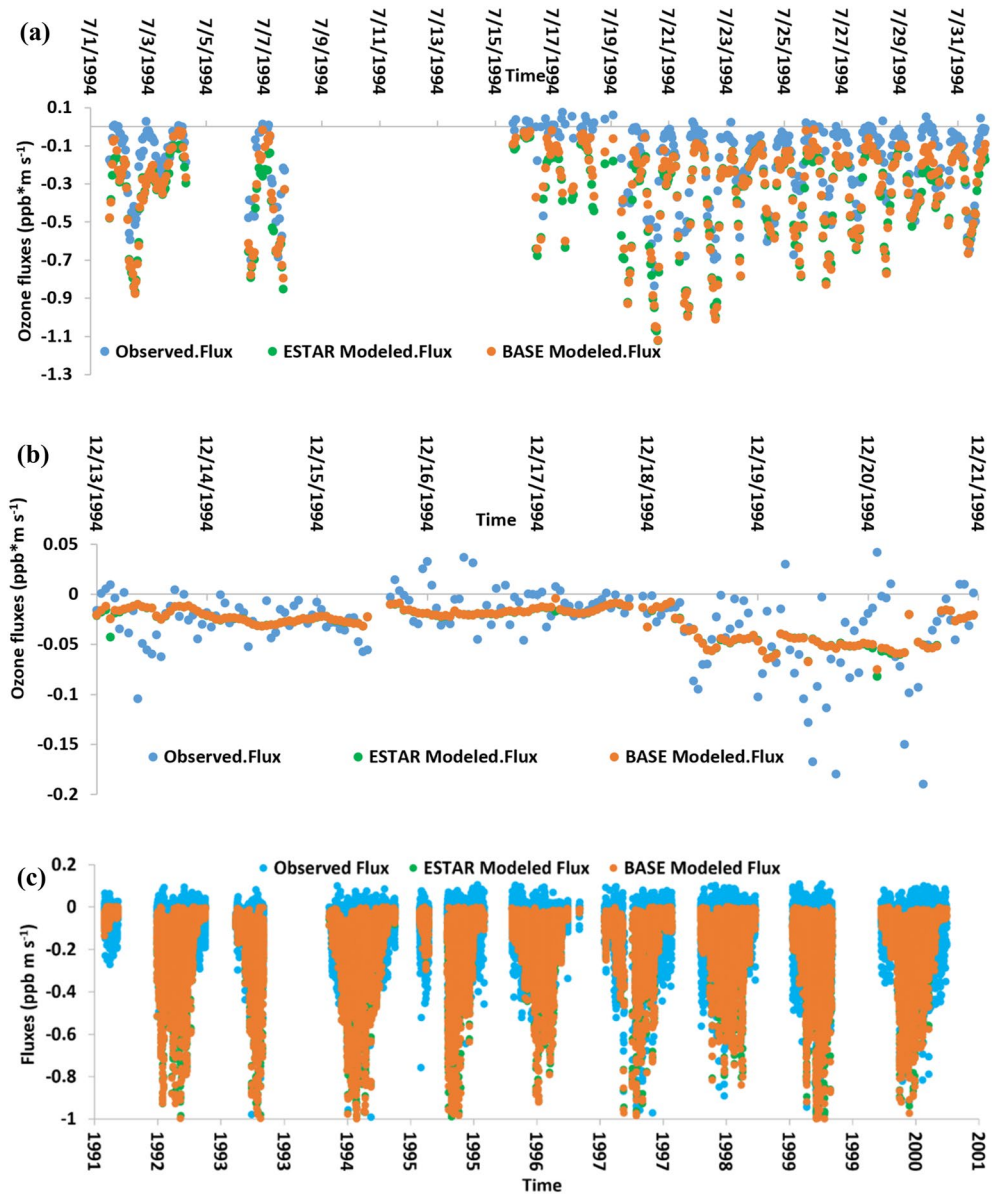

Figure 5. Temporal variation of modeled and observed O_3 kinematic fluxes (a) in July, (b) December 1994, and (c) for the entire decadal period for BASE, ESTAR, and OBS.

values indicate some uncertainty in measurements but to maintain consistency, we have included these positive fluxes in the model evaluation.

Simulated O_3 fluxes in BASE and ESTAR generally followed measured values and at times both overestimated (July, Figure 5a) and underestimated fluxes at times (December, Figure 5b) compared to measurements. However, both cases exhibited similar model performance in estimating O_3 fluxes. There is a remarkable similarity in the O_3 flux estimations during December in both cases. Decadal variation of estimated fluxes (Figure 5c) showed that during winter months both cases underestimated fluxes significantly as can be seen by clearly visible blue dots (measurements) that do not overlap with modeled values.

Figure 6a shows scatter plot of BASE *vs.* ESTAR for estimated O_3 fluxes for the decadal simulation period indicating a good alignment with each other with a R^2 of 0.99 and a slope of about 1.01, which confirmed that our new resistance formulations (ESTAR) performed as well as the standard STAGE deposition model (BASE). Ozone kinematic fluxes between the ranges of about 0–0.25 (ppb*m s^{-1}) in ESTAR are slightly higher than that

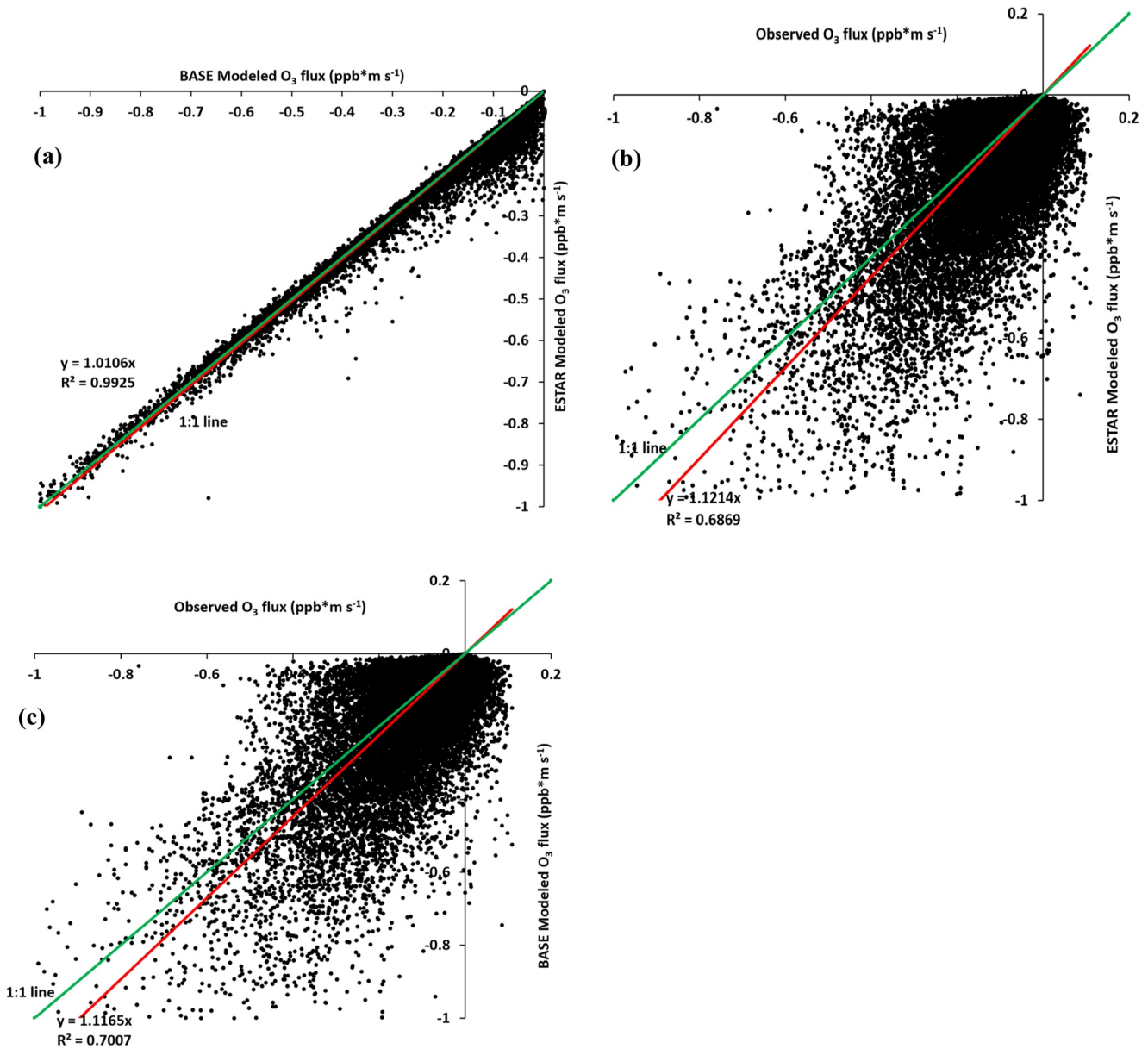

Figure 6. Scatter plot of (a) ESTAR *vs.* BASE modeled O_3 fluxes, (b) ESTAR *vs.* observed O_3 fluxes, and (c) BASE *vs.* observed O_3 fluxes for the decadal period (1991–2000).

in the BASE indicating turbulence modeled in ESTAR is slightly higher than that in BASE and is likely occurring during weakly unstable to stable conditions. This result can be attributed to the fact that, for stable conditions as discussed earlier, about 10% of decadal data for measured frication velocity (e_*-*obs*) is below 0.1 (m s^{-1}) (Figure S7 in the Supporting Information S1) while e_* was never below 0.1 (m s^{-1}). Results for calculated e_* contains no values less than 0.1 ms^{-1} may be attributed to the constants and bulk parameters used for e_* calculation. The rationale is that the constants a, b, and c used in the estimation of e_* are directly based on several special measurements where these constants were developed to possibly include transport processes occurred during those field measurements. In a way, this is good news for modelers because in models when u_* becomes less than 0.1, it is usually set to 0.1. This constraint is needed since very small values leads to modeled ozone being titrated out by NO_X leaving zero ozone in the surface layer during nighttime. This is a key problem in models when u_* is not constrained during model simulations. On the other hand, while e_* is naturally >0.1, it should help to improve air quality model simulations during stable PBL conditions.

Table 2
Statistical Performance of the Single-Point Model in Estimating O_3 Fluxes

Cases	NMB	NME	R	Number of data points
BASE	0.4270	−0.8000	0.7045	24,183
ESTAR	0.4798	−0.8513	0.6855	24,183

Scatter plot of ESTAR *vs.* OBS (Figure 6b) indicated a R^2 of about 0.69 with a slope of about 1.1, which includes positive fluxes that reflect measurement uncertainty. The positive O_3 fluxes may be attributed to some random variability in the measured flux. When magnitude of O_3 fluxes or vertical velocity fluctuations get very small, the signal to noise can get worse and can lead to the positive values even when the average flux should be zero over a period of time. Estimated fluxes between the ranges of about −0.2 to −0.6 in ESTAR are much higher than OBS, most likely due to intense turbulence represented in ESTAR. However, similar results are also found in BASE (shown in Figure 6c). Statistical performance of BASE and ESTAR decadal simulations is shown in Table 2.

In general, the NMB, NME, and R values of O_3 fluxes are also closer to each other for BASE and ESTAR, which is also indicative of the similar model performance for both cases while BASE has slightly smaller biases. Decadal statistical analysis for the diurnal and monthly model performance was also shown in Figures S6 of the Supporting Information S1, both cases exhibited similar model performance at different hours of day and in different months of year. Similar to that found with LHF estimations, differences between BASE and ESTAR in the decadal averages of diurnal variation for NMB, NME, and R are confined to nighttime while such differences for monthly variation are present during warmer months. Nighttime measurements are likely to have a greater uncertainty and may be less reliable because the assumptions that vertical turbulent transport dominates canopy-atmosphere exchange are not valid in the stable nocturnal surface layer.

4.2. Diurnal and Monthly Variations of Ozone Kinematic Fluxes

Figure 7 shows decadal averaged diurnal and monthly variation of simulated O_3 fluxes in BASE and ESTAR and corresponding measurements (OBS). Throughout the diurnal period estimated fluxes by ESTAR are very close to or slightly higher than BASE and both cases overestimated maximum values of fluxes compared to measured values. Such overestimation is quite large during daytime and can be attributed to uncertainties in resistance formulations and formulation chosen for each process among available multiple representation choices. On the other hand, decadal averaged O_3 fluxes are underpredicted during cooler months with overprediction during warmer months. It is likely that a large portion of ozone flux biases can be attributed to other resistances (e.g., nonstomatal) and since we did not propose any new formulations for those resistances. For this reason, we only study the uncertainties arising from the proposed new formulations in the next section. It is important to note that though Harvard Forest was generally considered to be adequately well watered and not have moisture stress, there may still be some level of modulation of stomatal conductance due to dew formation and particle (aerosol) blockage of stoma. In the follow-up near future work, we would consider this important point in evaluating stomatal and non-stomatal resistances.

As for the monthly variations of the O_3 fluxes (Figure 7b), when compared to OBS, both BASE and ESTAR estimated the seasonal patterns of O_3 fluxes well with higher fluxes during warmer months (June, July, and August, September) and lower fluxes during colder months (March, April, May, October, November, and December), respectively. In addition, both BASE and ESTAR had very close model performance in the modeling of O_3 fluxes. Also, data distributions for both cases for each month exhibited similar interquartile ranges as well as maximum, minimum, and median values. Analysis of all results indicated that the seasonality of the modeled O_3 fluxes arises from the seasonal variations of various resistances defined in STAGE model except for aerodynamic conductance, G_a, that has no clear seasonal cycle while rest of the resistances did show seasonal cycle. Small portions of these differences in the model performance of estimating O_3 fluxes were attributed to the differences in the calculation of various resistances, and the deposition velocity through each conductance is discussed in the following sections. Since the LHF are well simulated (Table 1, NMB < 20%), it can be said that the stomatal resistance as well as other resistances used in the LHF estimation are well characterized. Thus, large errors in the O_3 fluxes may be related to biases in the estimation of other resistances. However, that research is beyond the scope of this paper.

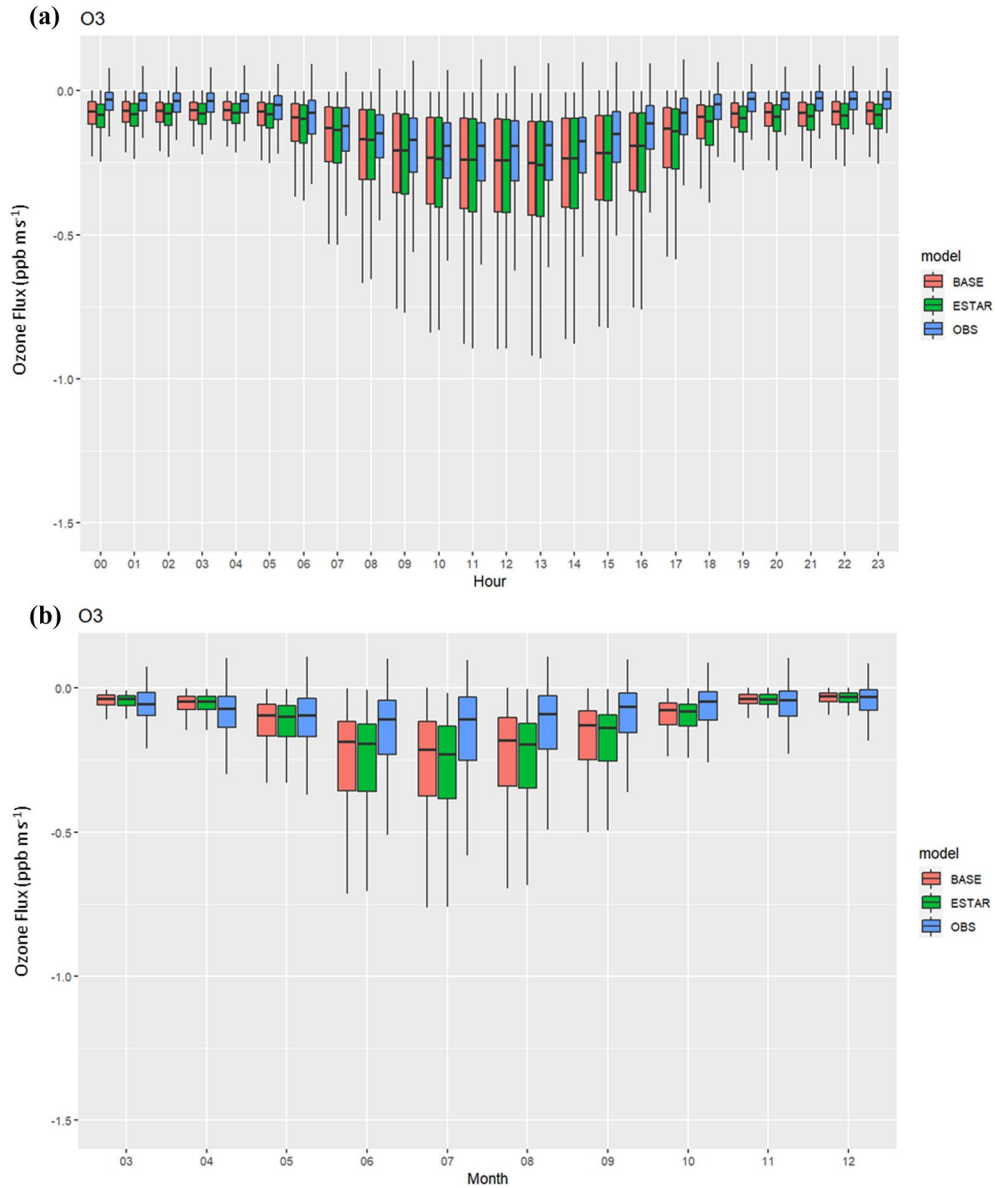

Figure 7. Decadal averages of (a) diurnal and (b) monthly variations of O_3 kinematic fluxes for BASE, ESTAR, and OBS.

4.3. Temporal Variation of Aerodynamic Conductance (G_a)

During strong surface heating conditions, typical of daytime in warmer periods, estimated aerodynamic conductance should be higher than those during cooler periods.

Long-term measurements-based estimation of aerodynamic conductance for heat at canopy and leaf scale (Kumagai et al., 2004; Mallick et al., 2018) indicated a general maximum value of 0.20 m s^{-1} with a maximum value of about 0.12 m s^{-1} at the highest probability density for a forest site (Panwar et al., 2020). In this study, both July and December values are well within the measured values documented in the literature. At times for two months (Figures 8a and 8b) BASE has slightly higher/lower values (~0.05) than ESTAR but in general the trends in both cases are very similar. Also, it can be seen that small G_a values in BASE are consistently lower than those in ESTAR and is directly related to smaller friction velocity values (<0.1 m s^{-1}) in the measurements. To further explore this variability between the cases, we show a scatter plot of aerodynamic conductance for BASE and ESTAR in Figure S9 of the Supporting Information S1. It can be seen that the aerodynamic conductances estimated by ESTAR are well within the 0–0.25 m s^{-1} range (with exception to few points) while

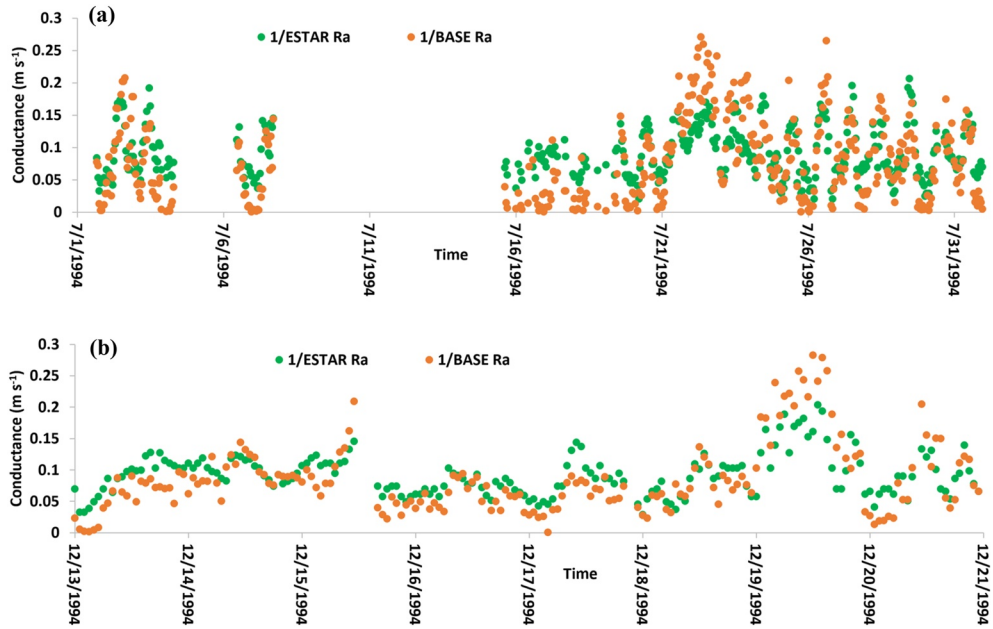

Figure 8. Temporal variation of modeled aerodynamic conductance (G_a) (a) July and (b) December 1994 for BASE and ESTAR.

in BASE several values are almost double of the values estimated by ESTAR. Based on the literature (Kumagai et al., 2004; Mallick et al., 2018), there is a possibility that several high conductance values in BASE may be an overestimation. Also, as discussed earlier, about 10% of observed u_{*_c} values are below 0.1 m s^{-1} (Figure S7 in the Supporting Information S1) and at times approaching zero values. Since the square of u_* is in the denominator in R_a calculation for BASE, small u_* values become much smaller leading to very small (closer to zero) values of conductance in BASE, as indicated by a large number of points at zero line of Y-axis (Figure S7 in the Supporting Information S1). In ESTAR, we observed no e_* values less than 0.1 for the entire simulation period.

4.4. Temporal Variation of Leaf Boundary Layer Conductance

As expected, leaf boundary layer conductance ($1/R_{blf}$) shown in Figure 9 is higher in summer periods than in winter except for few days in winter period, which was consistent with the monthly variation of leaf boundary layer conductance (not shown) though there are no leaves during winter season in this deciduous-dominated forest. Furthermore, diurnal variation of leaf boundary layer conductance can also be seen with higher values during daytime and lower values in nighttime in July with minimum values in BASE smaller than that in ESTAR. In general, both BASE and ESTAR exhibited similar diurnal and seasonal pattern. Scatter plot of leaf boundary layer conductance for BASE and ESTAR indicated similar feature, the regression line has a slope of 0.97 and R^2 of 0.96 (Figure S9 in the Supporting Information S1).

4.5. Temporal Variation of Soil Boundary Layer Conductance

Temporal variation of soil boundary layer conductance in July and December shown in Figure 10 is very similar for BASE and ESTAR. In addition, soil boundary layer conductance values are higher in winter than summer possibly due to snow cover as well as lack of leaves or small to zero LAI. Unlike the aerodynamic conductance, for both the boundary layer conductances atmospheric turbulence plays a secondary role, thus leading to the striking similarity in magnitude and variability of these two resistances in BASE and ESTAR. In addition to the seasonal pattern, soil boundary layer conductance also exhibited a diurnal variation with higher values during daytime and lower values during nighttime specifically in warmer months, and this may be attributed to the temperature-sensitive diffusivity of O_3; the diffusivity is higher for higher air temperatures due to the faster molecule movement. The scatter plot of soil boundary layer conductance for BASE and ESTAR showed a regression

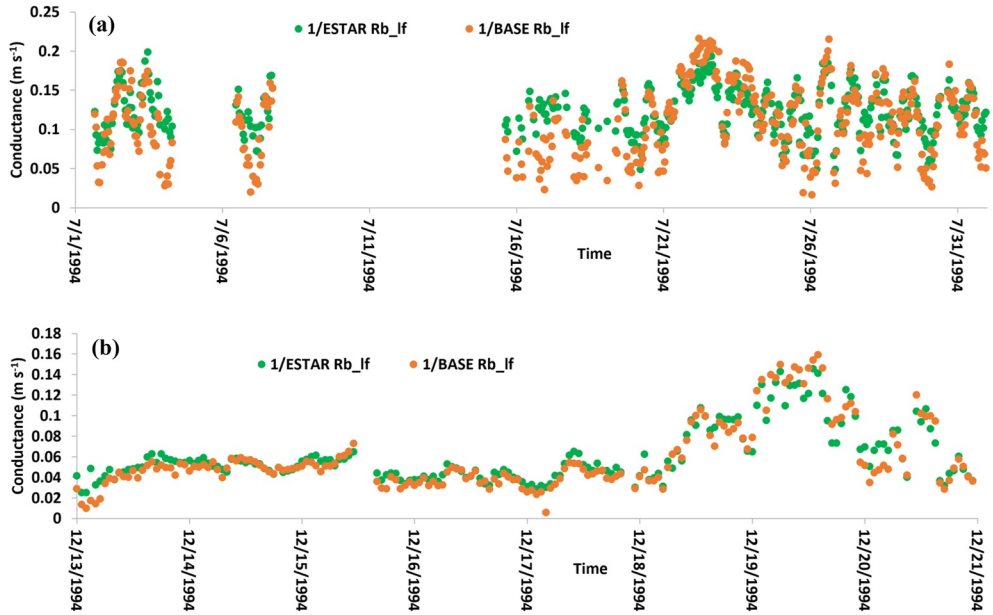

Figure 9. Temporal variation of modeled leaf boundary layer conductance ($1/R_{blf}$) in (a) July and (b) December 1994 for BASE and ESTAR.

line with slop of 1.01 and R^2 of 0.96 (Figure S9 in the Supporting Information S1), which is also strong evidence of good consistency of both cases for soil boundary layer conductance.

4.6. Temporal Variation of In-Canopy Conductance

Since in-canopy conductance values are estimated using the aerodynamic conductance values, variations in in-canopy conductance also followed the diurnal and seasonal variations of aerodynamic conductance with

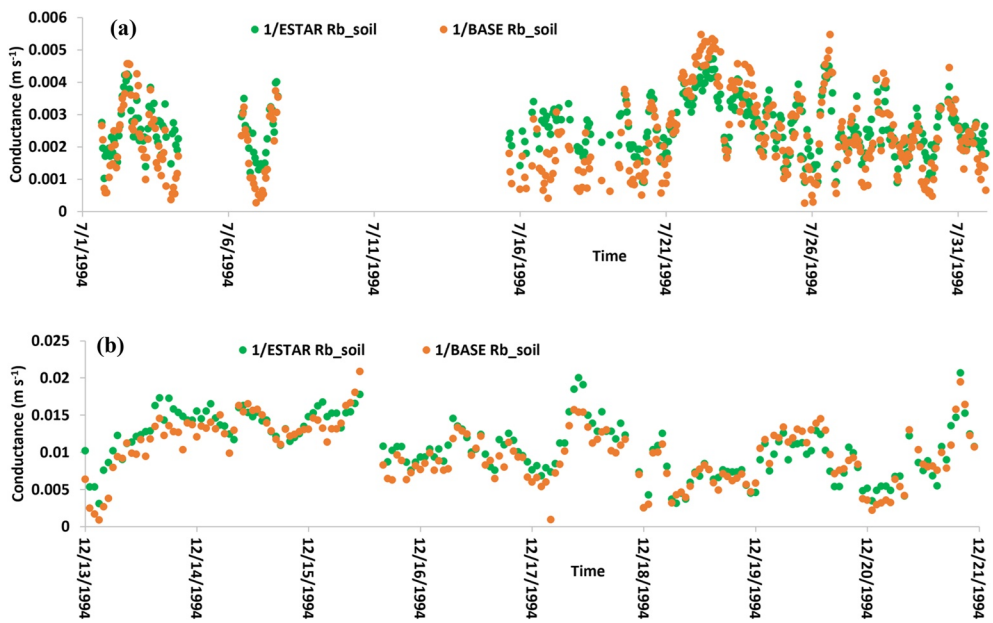

Figure 10. Temporal variation of modeled soil boundary layer conductance ($1/R_{bsoil}$) in (a) July and (b) December 1994 for BASE and ESTAR.

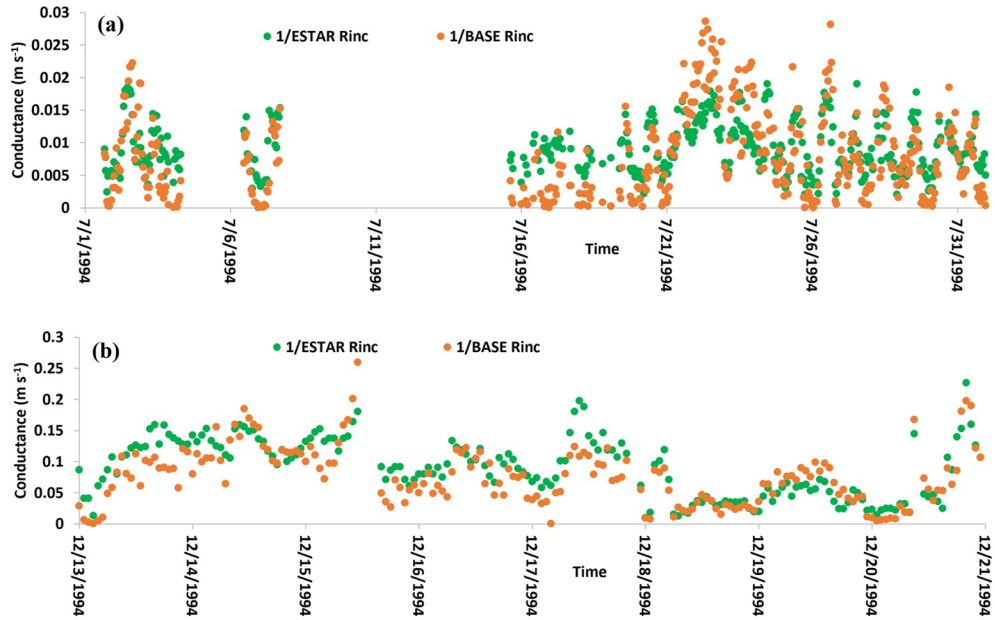

Figure 11. Temporal variation of in-canopy conductance ($1/R_{inc}$) in (a) July and (b) December 1994 for BASE and ESTAR.

higher values during daytime and lower values during nighttime shown in Figure 11a for July and the patterns in December are typical of winter conditions shown in Figure 11b.

4.7. Deposition Velocity

One of the most important aspects in air quality modeling is the estimation of V_d, which determines the magnitude of deposition to the underlying surface. Since dry deposition velocity inferred from measurements can be uncertain and is not a measured parameter, we analyze a scatter plot of estimated V_d for O_3 in BASE and ESTAR (Figure 12a). There is an excellent correlation between the two cases and the regression line has a slope of about 1.02 and R^2 of about 0.99.

As mentioned earlier, since observed u_{*_c} has values below 0.1 m s^{-1} for 10% of the decadal time period (Figure S7 in the Supporting Information S1), it has resulted in a skewed relationship with V_d values for ESTAR that were below 0.004 m s^{-1} (see the circled area in Figure 12a). Simulations using only u_{*_c} values less than 0.1 m s^{-1}

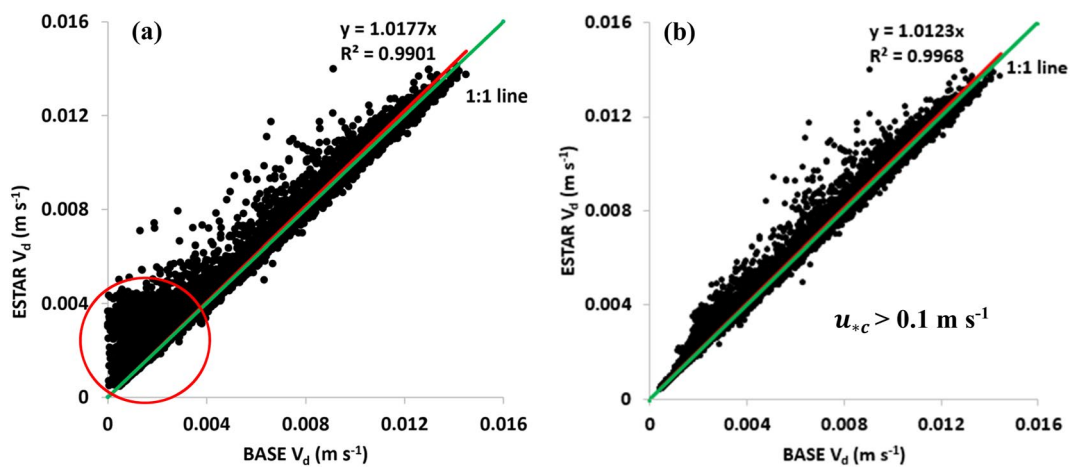

Figure 12. Scatter plot of ESTAR vs. BASE modeled deposition velocity for the decadal period (1991–2000), (a) the whole dataset, (b) the dataset when $u_{*_c} > 0.1$ m s^{-1}

confirmed the contributions of small u_{*_c} values (<0.1 m s^{-1}) to the skewed relationship between V_d values for BASE and ESTAR (not shown). Then, we limited the u_{*_c} values not to be less than 0.1 m s^{-1} in another model simulation of the BASE and the results are shown in Figure 12b. The skewness shown in Figure 12a has disappeared and in general, the V_d values for both cases aligned with each other well, even when the values were greater than 0.004 m s^{-1}. The good agreement of V_d values between BASE and ESTAR indicates that the new model formulations used in the ESTAR are able to perform as good as original formulations that used measured friction velocity in the single-point model.

To make sure that we have properly implemented all new formulations into the single-point model, we have analyzed the scatter plots for stomatal, cuticle, and soil conductances in BASE and ESTAR and these are shown in Figure S10 of the Supporting Information S1. Since stomatal conductance uses aerodynamic conductance (see Text S3 of the Supporting Information S1), scatter plot indicates minor differences between the BASE and ESTAR stomatal conductance. Scatter plots for cuticle and soil conductances indicate no differences confirming that our implementation of new formulations is correctly done in the single-point model.

5. Sensitivity Studies

Though the main focus of this paper is on proposing and validating the turbulence velocity scale for use in dry deposition estimation, we present here some sensitivity studies related to the four resistance formulations that were evaluated using the new velocity scale. This additional study was prompted by the fact that the diurnal variation of modeled O_3 dry deposition fluxes in BASE and ESTAR showed biases when compared to OBS (daytime maximum overestimation error is about 20%–30%). Thus, we performed one sensitivity study through the consideration of uncertainty range for crucial parameter(s) in those resistance formulations. Though uncertainty can exist in other resistance formulations (e.g., stomatal resistance) as well as from the choice of options to choose from representing different processes and inputs, and since we have not proposed new formulations for other resistances (e.g., stomatal and non-stomatal resistances), we will revisit a full-scale uncertainty estimation analysis in a near future study when presenting such new formulations for the rest of the resistances. Thus, we consider here additional simulations only related to uncertainty in the proposed four resistance formulations.

The aerodynamic resistance is based on measured wind speed and friction velocity and the analysis of both parameters was presented earlier using Equation 5 and measured wind speed. We infer that the uncertainty present in the estimation of R_a can be small with an exception to the measured friction velocity being very high during strong local heating at the surface and may not warrant further scrutiny. Also, Equation 6 performed well in comparison with Equation 5, thus we will focus on the other three resistances formulations. These are: leaf and soil boundary layer resistances and in-canopy aerodynamic resistance shown in Equations 10–12. The common parameter that can potentially have some uncertainty is LAI because of its spatial heterogeneity across the Harvard Forest site. LAI uncertainty study (e.g., Richardson et al., 2011) for Ameriflux sites indicated that uncertainties in optical measurements of LAI were found to be about 5%–10% depending upon choice of measuring instrument that was used while data processing error could be around 10%–20%. Because of the spatial heterogeneity of LAI for the Harvard Forest site, the standard error can be as much as 20% (analysis data obtained for the Harvard Forest site) (Munger & Wofsy, 2021). Note that for the sake of convenience we are referring to the measured *plant-area index* as LAI since it includes branches and needles as well as the leaves (anything that attenuates light). Given these estimates of uncertainty, we have designed two sensitivity studies where LAI in Equations 10–12 was decreased by 20% (referred to as (0.8LAI) and increased by 20% (referred to as 1.2LAI) to study the cumulative effects of LAI uncertainty on the modeled O_3 fluxes. Figure 13 shows diurnal variation of simulated O_3 fluxes averaged at decadal scale for OBS, ESTAR, 0.8LAI, and 1.2LAI cases.

There exist only small O_3 flux differences among the cases, indicating the uncertainty in the specification of LAI in the three resistances (Equations 10–12) is not a major player in the total bias existed in the O_3 flux estimations while such bias could be arising from other resistances or from other sources. Interestingly, those small differences (∼) 0.02 ppb m s^{-1} among the maximum values of simulated fluxes do not vary linearly in time. This feature can be related back to the nonlinearity in the usage of LAI in those equations.

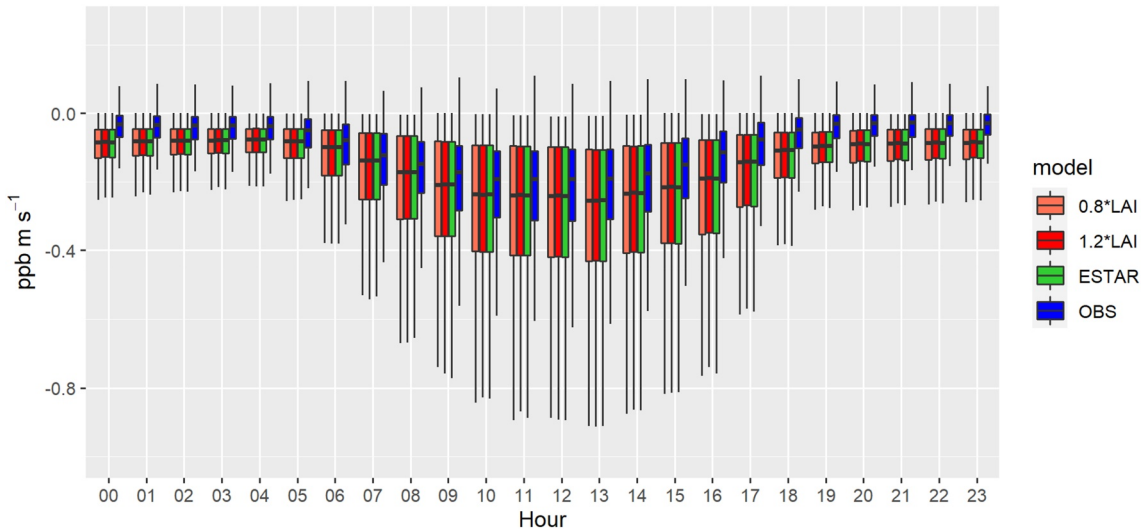

Figure 13. Decadal averages of diurnal variations of O_3 kinematic fluxes for OBS, ESTAR, 0.8LAI, and 1.2LAI cases.

6. Conclusions

Atmospheric turbulence is a process that significantly contributes to the dry deposition. It is intuitive to consider 3-D turbulence information in estimating relevant resistances, but no such methods exist. Thus, there is a need for 3-D turbulence velocity scale to (a) avoid using different stability functions that can be sources of biases and/or differences among different model's deposition estimations; and (b) improve turbulence strength representation in resistance formulations. By approximating surface TKE, a turbulence velocity scale (e_*) inclusive of 3-D turbulence generated during different conditions in the PBL has been parameterized and validated for use with resistance formulations that are dependent on atmospheric turbulence. Then, we hypothesized and validated that measured friction velocity (that includes vertical heat flux impacts on vertical transport of horizontal momentum flux) can be approximated by the product of von Karman constant (k) and the new velocity scale (i.e., as ke_*). Then, we proposed a new approach where friction velocity has been replaced by the ke_* in several resistance formulations. Using the single-point version of the STAGE deposition model, we have simulated the surface latent heat and ozone fluxes for a decade at Harvard Forest site and evaluated the model performance based on our newly proposed as well as the existing resistance formulations. Results indicated that the parameterized new velocity scale has R^2 of about 0.96 when compared to that measured by the 3-D sonic anemometer, providing solid foundation for the use of e_* in dry deposition modeling. We also found that the measured friction velocity by a 3-D sonic anemometer has a R^2 of about 0.94 when compared to the product ke_*. These results allowed us to effectively replace the measured friction velocity by the product of von Karman constant and turbulence velocity scale. Other results indicated that the new formulations work very well in simulating surface latent heat and ozone fluxes when compared to respective measurements at decadal time scale. Simulations performed in this study provided an opportunity to evaluate hourly and seasonal performances of the new formulations for four resistances at a decadal time scale as these four resistances play different roles in determining the dry deposition depending upon the time of a day and season. We conclude that:

1. The usage of e_* in resistance formulations is consistent with its counterpart, friction velocity measured by 3-D sonic anemometer, in the observation-driven single-point models since both include contributions from vertical heat fluxes.
2. Since 3-D sonic anemometer measurements are not available at routine surface measurement sites, e_* was estimated using bulk boundary layer parameters that are readily available/estimated from routine surface measurements. Thus, e_* helps to replicate 3-D sonic anemometer measured by friction velocity in models for use by the scientific community across the globe. This feature helps to avoid the usage of stability functions explicitly in models, which contribute to differences among different models' predictions.
3. Though the present study used only one observational site, essentially our decadal timescale study implicitly contains spatial heterogeneity because of time-space equivalence. However, a 3-D air quality modeling studies

are warranted to further validate these new formulations and also to determine whether there is any primary role for friction velocity for deposition modeling.

4. Generally, stability correction formulations are used only in aerodynamic resistance estimation and also in particle deposition schemes but not in all turbulence-dependent resistances. However, usage of our new velocity scale naturally brings in stability-dependent turbulence effects in many resistance formulations for different regimes of boundary layer.
5. A new equation for log-law based on new velocity scale for estimating surface wind speed without explicitly using any stability functions has been validated and it can be further tested for use in surface layer meteorological modeling.

We are cognizant of the fact that an important question for deposition of many trace gases can still be about our ability to accurately model the surface uptake properties represented by stomatal and non-stomatal conductances, and that topic will be the focus of our near-future research. Accurate atmospheric deposition modeling can help develop global and regional maps of total atmospheric deposition to identify risky areas that would benefit from effective measures to control pollutant emissions as well as to develop air quality management strategies and regulatory policies. The findings from this research may help improve the capability of dry deposition scheme for better estimating the dry deposition fluxes. . In the companion paper (Part-2), we have addressed some issues related to turbulence strength representation in particle deposition schemes. Our near-future work will (a) test the performance of new resistance formulations in estimating dry deposition fluxes of other and reactive gas pollutants such as ammonia (NH_3) and nitric acid (HNO_3); and (b) extend this research to stomatal and non-stomatal resistances. Then, our final goal is to apply these new formulations in the Community Multiscale Air Quality model to test their performance at regional and hemispheric scales.

Data Availability Statement

All modeling codes and data associated with the study including figures and tables shown in this article can be freely downloaded at: http://doi.org/10.5281/zenodo.5874971.

Acknowledgments

The research was partially and internally funded by the U.S. EPA. Our sincere gratitude goes to Mr. John M. Southerland, Jr. for kindly supporting the research. The authors are thankful to Drs. Christian Hogrefe and Zhiyong Wu and two anonymous reviewers for providing very helpful comments that improved the quality of this paper. Authors appreciates scientific help provided by the AQMEII4 dry deposition group, in particular Drs. Olivia Clifton and Donna Schwede for giving access to all needed data. The authors thank Mrs. Pooja Alapaty for technical editing of the manuscript. The views expressed in this article are those of the author(s) and do not necessarily represent the views or the policies of the U.S. Environmental Protection Agency. Harvard Forest observations were supported in part by the U.S. Department of Energy, Office of Science (BER), and National Science Foundation Long-Term Ecological Research.

References

Alapaty, K., & Alapaty, M. (2001). Evaluation of a nonlocal-closure K-scheme using the MM5, 11th Annual Penn State/NCAR MM5 Users' Workshop, Boulder, CO. Retrieved from http://www2.mmm.ucar.edu/mm5/workshop/ws01/alapaty1.pdf

Appel, K. W., Bash, J. O., Fahey, K. M., Foley, K. M., Gilliam, R. C., Hogrefe, C., et al. (2021). The Community Multiscale Air Quality (CMAQ) model versions 5.3 and 5.3.1: System updates and evaluation. *Geoscientific Model Development*, *14*(5), 2867–2897. https://doi.org/10.5194/gmd-14-2867-2021

Barford, C. C., Wofsy, S. C., Goulden, M. L., Munger, J. W., Pyle, E. H., Urbanski, S. P., et al. (2001). Factors controlling long- and short-term sequestration of atmospheric CO_2 in a midlatitude forest. *Science*, *294*(5547), 1688–1691. https://doi.org/10.1126/science.1062962

Bash, J. O., Cooter, E. J., Dennis, R. W., Walker, J. T., & Pleim, J. E. (2013). Evaluation of a regional air-quality model with bi-directional NH_3 exchange coupled to an agro-ecosystem model. *Biogeosciences*, *10*(3), 1635–1645. https://doi.org/10.5194/bg-10-1635-2013

Boose, E., & Gould, E. (1999). Shaler meteorological station at Harvard Forest 1964–2002. *Harvard Forest data archive*, HF000. https://doi.org/10.6073/pasta/84cf303ea3331fb47e8791aa61aa91b2

Brenner, A. J., & Jarvis, P. G. (1995). A heated leaf replica technique for determination of leaf boundary layer conductance in the field. *Agricultural and Forest Meteorology*, *72*, 261–275. https://doi.org/10.1016/0168-1923(94)02160-l

Clifton, O. E., Fiore, A. M., Massman, W. J., Baublitz, C. B., Coyle, M., Emberson, L., et al. (2020). Dry deposition of ozone over land: Processes, measurement, and modeling. *Reviews of Geophysics*, *58*(1), e2019RG000670. https://doi.org/10.1029/2019RG000670

Clifton, O. E., Fiore, A. M., Munger, J. W., Malyshev, S., Horowitz, L. W., Shevliakova, E., et al. (2017). Interannual variability in ozone removal by a temperate deciduous forest. *Geophysical Research Letters*, *44*(1), 542–552. https://doi.org/10.1002/2016GL070923

Clifton, O. E., Fiore, A. M., Munger, J. W., & Wehr, R. (2019). Spatiotemporal controls on observed daytime ozone deposition velocity over northeastern U.S. forests during summer. *Journal of Geophysical Research: Atmospheres*, *124*, 5612–5628. https://doi.org/10.1029/2018JD029073

Deardorff, J. W. (1974). Three-dimensional numerical study of the height and mean structure of a heated planetary boundary layer. *Boundary-Layer Meteorology*, *7*, 81–106. https://doi.org/10.1007/BF00224974

El-Madany, T. S., Niklasch, K., & Klemm, O. (2017). Stomatal and non-stomatal turbulent deposition flux of ozone to a managed peatland. *Atmosphere*, *8*(9), 175. https://doi.org/10.3390/atmos8090175

Emmerichs, T., Kerkweg, A., Ouwersloot, H., Fares, S., Mammarella, I., & Taraborrelli, D. (2021). A revised dry deposition scheme for land–atmosphere exchange of trace gases in ECHAM/MESSy v2.54. *Geoscientific Model Development*, *14*(1), 495–519. https://doi.org/10.5194/gmd-14-495-2021

Flechard, C. R., Nemitz, E., Smith, R. I., Fowler, D., Vermeulen, A. T., Bleeker, A., et al. (2011). Dry deposition of reactive nitrogen to European ecosystems: A comparison of inferential models across the NitroEurope network. *Atmospheric Chemistry and Physics*, *11*(6), 2703–2728. https://doi.org/10.5194/acp-11-2703-2011

Fuentes, J. D., Chamecki, M., Roulston, T., Chen, B., & Pratt, K. R. (2016). Air pollutants degrade flora scents and increase insect foraging times. *Atmospheric Environment*, *141*, 361–374. https://doi.org/10.1016/j.atmosenv.2016.07.002

Gates, D. M., & Benedict, C. M. (1962). Convection phenomena from plants in still air. *American Journal of Botany*, *50*(6), 563–573. https://doi.org/10.2307/2440031

He, J., & Alapaty, K. (2018). Precipitation partitioning in multiscale atmospheric simulations: Impacts of stability restoration methods. *Journal of Geophysical Research: Atmospheres*, *123*, 185–10. https://doi.org/10.1029/2018JD028710

Hicks, B. B. (1985). Behavior of turbulence statistics in the convective boundary layer. *Journal of Applied Meteorology and Climatology*, *24*, 607–614. https://doi.org/10.1175/1520-0450(1985)024<0607:botsit>2.0.co;2

Hogrefe, C., Galmarini, S., Solazzo, E., Bianconi, R., Bellasio, R., Liu, P., & Mathur, R. (2020). Continental-Scale Analysis of Atmospheric Deposition Over North America and Europe Using the AQMEII Database. In *Chapter 48, Air Pollution Modeling and its Application XXVI* (pp. 305–308). Springer Nature Group. https://doi.org/10.1007/978-3-030-22055-6_48

Iacono, M. J. (2011). Application of improved radiation modeling to General Circulation Models 12 August 2021. Retreived from https://core.ac.uk/download/pdf/207653486.pdf

Izumi, Y., & Caughey, J. S. (1976). *Minnesota 1973 atmospheric boundary layer experiment data report*. AFCRL-TR-.

Kessomkiat, W., Franssen, H.-J. H., Graf, A., & Vereecken, H. (2013). Estimating random errors of eddy covariance data: An extended two-tower approach. *Agricultural and Forest Meteorology*, *171*(172), 203–219. https://doi.org/10.1016/j.agrformet.2012.11.019

Kiefer, M. T., Lin, Y., & Charney, J. J. (2008). A study of two-dimensional dry convective plume models with variable critical level height. *Journal of the Atmospheric Sciences*, *65*(2), 448–469. https://doi.org/10.1175/2007JAS2301.1

Kumagai, T., Saitoh, T. M., Sato, Y., Morooka, T., Manfroi, O. J., Kuraji, K., & Suzuki, M. (2004). Transpiration, canopy conductance and the decoupling coefficient of a lowland mixed dipterocarp forest in Sarawak, Borneo: Dry spell effects. *Journal of Hydrology*, *287*, 237–251. https://doi.org/10.1016/j.jhydrol.2003.10.002

Liu, S., Lu, L., Mao, D., & Jia, L. (2007). Evaluating parameterizations of aerodynamic resistance to heat transfer using field measurements. *Hydrology and Earth System Sciences*, *11*(2), 769–783. https://doi.org/10.5194/hess-11-769-2007

Mailhot, J., & Benoit, R. (1982). A finite-element model of the atmospheric boundary layer suitable for use with numerical weather prediction models. *Journal of the Atmospheric Sciences*, *39*(10), 2249–2266. https://doi.org/10.1175/1520-0469(1982)039<2249:afemot>2.0.co;2

Mallick, K., Wandera, L., Bhattarai, N., Hostache, R., Kleniewska, M., & Chormanski, J. (2018). A critical evaluation on the role of aerodynamic and canopy–surface conductance parameterization in SEB and SVAT models for simulating evapotranspiration: A case study in the Upper Biebrza National Park Wetland in Poland. *Water*, *10*(12), 1753. https://doi.org/10.3390/w10121753

Massad, R.-S., Nemitz, E., & Sutton, M. A. (2010). Review and parameterization of bi-directional ammonia exchange between vegetation and the atmosphere. *Atmospheric Chemistry and Physics*, *10*(21), 10359–10386. https://doi.org/10.5194/acp-10-10359-2010

McMillen, R. T. (1988). An eddy correlation technique with extended applicability to non-simple terrain. *Boundary-Layer Meteorology*, *43*, 231–245. https://doi.org/10.1007/BF00128405

Moore, K. E., Fitzjarrald, D. R., Sakai, R. K., Goulden, M. L., Munger, J. W., & Wofsy, S. C. (1996). Seasonal variation in radiative and turbulent exchange at a deciduous forest in central Massachusetts. *Journal of Applied Meteorology*, *35*(1), 122–134. https://doi.org/10.1175/1520-0450(1996)035<0122:svirat>2.0.co;2

Munger, J. W., Fan, S.-E., Bakwin, P. S., Goulden, M. L., Goldstein, A. H., Colman, A. S., & Wofsy, S. C. (1998). Regional budgets for nitrogen oxides from continental sources: Variations of rates for oxidation and deposition with season and distance from source regions. *Journal of Geophysical Research*, *103*(D7), 8355–8368. https://doi.org/10.1029/98JD00168

Munger, J. W., Wofsy, S. C., Bakwin, P. S., Fan, S.-M., Goulden, M. L., Daube, B. C., et al. (1996). Atmospheric deposition of reactive nitrogen oxides and ozone in a temperate deciduous forest and a subarctic woodland 1. Measurements and mechanisms. *Journal of Geophysical Research*, *101*(D7), 12639–12657. https://doi.org/10.1029/96JD00230

Munger, W., & Wofsy, S. (2021). *Biomass inventories at Harvard Forest EMS tower since 1993* (p. HF069). Harvard Forest Data Archive. (v.36Environmental Data Initiative: https://doi.org/10.6073/pasta/5c2f17c295413da2a2a091fd7696af40

Nemitz, E., Milford, C., & Sutton, M. A. (2001). A two-layer canopy compensation point model for describing bi-directional biosphere-atmosphere exchange of ammonia. *Quarterly Journal of the Royal Meteorological Society*, *127*(573), 815–833. https://doi.org/10.1002/qj.49712757306

Otte, T. L., Nolte, C. G., Otte, M. J., & Bowden, J. H. (2012). Does nudging squelch the extremes in regional climate modeling? *Journal of Climate*, *25*(20), 7046–7066. https://doi.org/10.1175/JCLI-D-12-00048.1

Padro, J., den Hartog, G., & Neumann, H. H. (1991). An investigation of the ADOM dry deposition module using summertime O3 measurements above a deciduous forest. *Atmospheric Environment*, *25*, 1689–1704. https://doi.org/10.1016/0960-1686(91)90027-5

Panwar, A., Renner, M., & Kleidon, A. (2020). Imprints of evaporative conditions and vegetation type in diurnal temperature variations. *Hydrology and Earth System Sciences*, *24*(10), 4923–4942. https://doi.org/10.5194/hess-24-4923-2020

Personne, E., Loubet, B., Herrmann, B., Mattsson, M., Schjoerring, J. K., Nemitz, E., et al. (2009). SURFATM-NH3: A model combining the surface energy balance and bi-directional exchanges of ammonia applied at the field scale. *Biogeosciences*, *6*(8), 1371–1388. https://doi.org/10.5194/bg-6-1371-2009

Pleim, J., & Ran, L. (2011). Surface flux modeling for air quality applications. *Atmosphere*, *2*(3), 271–302. https://doi.org/10.3390/atmos2030271

Pleim, J., Ran, L., Appel, W., Shephard, M. W., & Cady-Pereira, K. (2019). New bidirectional ammonia flux model in an air quality model coupled with an agricultural model. *Journal of Advances in Modeling Earth Systems*, *11*(9), 2934–2957. https://doi.org/10.1029/2019MS001728

Pye, H. O. T., Seltzer, K., Murphy, B., Allen, C., Piletic, I., D'Ambro, E., et al. (2021). *Integrating reactive organic carbon emissions into the Community Regional Atmospheric Chemistry Multiphase Mechanism (CRACMM), presentation at the CMAS Conference*. Chapel Hill, NC and International Aerosol Modeling Algorithms Conference.

Richardson, A. D., Dail, D. B., & Hollinger, D. Y. (2011). Leaf area index uncertainty estimates for model–data fusion applications. *Agricultural and Forest Meteorology*, *151*, 1287–1292. https://doi.org/10.1016/j.agrformet.2011.05.009

Richardson, A. D., Hollinger, D. Y., Burba, G. C., Davis, K. J., Flanagan, L. B., Katul, G. G., et al. (2006). A multi-site analysis of random error in tower-based measurements of carbon and energy fluxes. *Agricultural and Forest Metereology*, *136*(1–2), 1–18. https://doi.org/10.1016/j.agrformet.2006.01.007

Stella, P., Personne, E., Loubet, B., Lamaud, E., Ceschia, E., Beziat, P., et al. (2011). Predicting and portioning ozone fluxes to maize crops from sowing to harvest: The Surfatm-O3 model. *Biogeosciences*, *8*(10), 2869–2886. https://doi.org/10.5194/bg-8-2869-2011

Toyota, K., Dastoor, A. P., & Ryzhkov, A. (2016). Parameterization of gaseous dry deposition in atmospheric chemistrymodels: Sensitivity to aerodynamic resistance formulations understatically stable condition. *Atmospheric Environment*, *147*, 409–422. https://doi.org/10.1016/j.atmosenv.2016.09.055

Urbanski, S., Barford, C., Wofsy, S., Kucharik, C., Pyle, E., Budney, J., et al. (2007). Factors controlling CO_2 exchange on timescales from hourly to decadal at Harvard Forest. *Journal of Geophysical Research*, *112*, G02020. https://doi.org/10.1029/2006JG000293

Walker, J. T., Beachley, G. M., Amos, H. M., Baron, J. S., Bash, J., Baumgardner, R., et al. (2019). *Science needs for continued development of total nitrogen deposition budgets in the United States*. U.S. Environmental Protection Agency. EPA 601/R-19/001.

Warner, J. (1972). The structure and intensity of turbulence in air over the sea. *Quarterly Journal of Royal Meteorological Society*, *98*(415), 175–186. https://doi.org/10.1002/qj.49709841514

Wesely, M. L. (1989). Parameterization of surface resistances to gaseous dry deposition in regional-scale numerical models. *Atmospheric Environment*, *23*(6), 1293–1304. https://doi.org/10.1016/0004-6981(89)90153-4

Wigley, G., & Clark, J. A. (1974). Heat transfer coefficients for constant energy flux models of broad leaves. *Boundary-Layer Meteorology*, *7*, 139–150. https://doi.org/10.1007/bf00227909

WMO (World Meteorological Organization). (2021). Atmospheric deposition. available at:(last access: https://public.wmo.int/en/our-mandate/focus-areas/environment/atmospheric-deposition 26 May 2021.

Wong, A. Y. H., Geddes, J. A., Tai, A. P. K., & Silva, S. J. (2019). Importance of dry deposition parameterization choice in global simulations of surface ozone. *Atmospheric Chemistry and Physics*, *19*(22), 14365–14385. https://doi.org/10.5194/acp-19-14365-2019

Wu, Z., Schwede, D. B., Vet, R., Walker, J. T., Shaw, M., Staebler, R., & Zhang, L. (2018). Evaluation and intercomparison of five North American dry deposition algorithms at a mixed forest site. *Journal of Advances in Modeling Earth Systems*, *10*(7), 1571–1586. https://doi.org/10.1029/2017ms001231

Wu, Z., Wang, X., Chen, F., Turnipseed, A. A., Guenther, A. B., Niyogi, D., et al. (2011). Evaluating the calculated dry deposition velocities of reactive nitrogen oxides and ozone from two community models over a temperate deciduous forest. *Atmospheric Environment*, *45*(16), 2663–2674. https://doi.org/10.1016/j.atmosenv.2011.02.063

Wyngaard, J. C. (1975). Modeling the planetary boundary layer-extension to the stable case. *Boundary-Layer Meteorology*, *9*, 441–460. https://doi.org/10.1007/BF00223393

Wyngaard, J. C., & Cote, O. R. (1974). The evolution of a convective planetary boundary layer-a higher-order-closure model study. *Boundary-Layer Meteorology*, *7*, 289–308. https://doi.org/10.1007/BF00240833

Zhang, L., Brook, J. R., & Vet, R. (2003). A revised parameterization for gaseous dry deposition in air-quality models. *Atmospheric Chemistry and Physics*, *3*(6), 2067–2082. https://doi.org/10.5194/acp-3-2067-2003

References From the Supporting Information

Britannica (2021). Coefficient of determination 12 August 2021. Retreived from https://www.britannica.com/science/coefficient-of-determination

Chang, J. C., & Hanna, S. R. (2004). Air quality model performance evaluation. *Meteorology and Atmospheric Physics*, *87*, 167–196. https://doi.org/10.1007/s00703-003-0070-7

Emery, C., Liu, Z., Russell, A. G., Odman, M. T., Yarwood, G., & Kumar, N. (2017). Recommendations on statistics and benchmarks to assess photochemical model performance. *Journal of the Air & Waste Management Association*, *67*(5), 582–598. https://doi.org/10.1080/10962247.2016.1265027